Title
K+ -NUCLEON INTERACTIONS IN THE MOMENTUM RANGE OF 800 to 2900 MeV/c

Author
Cook, Victor.

Publication Date
1962-03-21

UCRL-10130
Cy. 2

University of California

Ernest O. Lawrence Radiation Laboratory

Berkeley, California

DISCLAIMER

UCRL-10130
UC-34 Physics
TID-4500 (17th Ed.)

UNIVERSITY OF CALIFORNIA
Lawrence Radiation Laboratory
Berkeley, California

Contract No. W-7405-eng-48

K^+ NUCLEON INTERACTIONS IN THE MOMENTUM RANGE OF 800 to 2900 Mev/c

Victor Cook

(Thesis)

March 21, 1962

K^+ NUCLEON INTERACTIONS IN THE MOMENTUM RANGE OF 800 to 2900 Mev/c

Contents

K^+ NUCLEON INTERACTIONS IN THE MOMENTUM RANGE OF 800 TO 2900 Mev/c

Victor Cook

Lawrence Radiation Laboratory
University of California
Berkeley, California

March 21, 1962

ABSTRACT

Experimental measurements of the K^+-nucleon total cross section in the momentum range between 0.8 and 2.9 Bev/c, and K^+-proton elastic scattering angular distributions at 0.97, 1.17, and 1.97 Bev/c are reported.

The K^+-proton and K^+-neutron total cross sections were found to be nearly equal and constant at about 17.5 mb between 1.0 and 2.9 Bev/c. At 0.77 Bev/c both cross sections are significantly lower; the value measured for K^+-proton was 13 mb, and for K^+-neutron was about 15 mb.

Phase-shift analyses of the K^+-proton differential cross sections are discussed. Several sets of solutions found at 0.97 and 1.17 Bev/c are given. The angular distribution at 1.97 Bev/c is peaked in the forward direction, indicating the presence of many angular-momentum states. The results of an optical-model analysis of these data are presented.

The existing information on $K^\pm$-proton total cross sections and experimental values for the real part of the forward scattering amplitude were used in a forward-dispersion-relation calculation to evaluate the residue of the effective pole $\tilde{\Gamma}(\Lambda, \Sigma, Y_1^*, Y_0^*)$, and to compare the energy dependence of the real part of the forward scattering amplitude, as predicted by the forward dispersion relations, with the data.

I. INTRODUCTION

In the decade since the discovery of K mesons, many experimental studies have been undertaken to elucidate the nature of their interactions with nucleons (N), and to determine their intrinsic properties. A great body of experimental data has been accumulated,[1] and several theories of the K-N interaction have been proposed.[2] However, none of these theories has succeeded in satisfying all of the empirical data. This situation is, of course, not unique with K-N interactions, but rather is typical of all strange-particle interactions.

The dispersion-relation (S-matrix) theory of strong interactions seems to be the most promising at the present time.[3] The strange-particle dispersion relations have not been completely justified;[4] however, several authors have proceeded by analogy with the π-N case to derive and use K-N dispersion relations.[5,6] The approximations and assumptions necessary to derive these expressions can, in principle, be checked by comparing the predictions of the theory with the experimental data.

In recent applications of the S-matrix theory to the K-N problem, forward-scattering dispersion relations have been used in an attempt to deduce the K-N-hyperon relative parity, and the interaction coupling constants.[7,8] However, it has not been possible to arrive at a unique solution, partly because of the lack of experimental data at high energies.

Experimental information prior to the experiment reported herein showed the K^+-p total cross section rising slowly from about 10 mb at low energies up to about 13 mb at p(lab) = 1.0 Bev/c.[9,10] Measurements at higher momenta indicated the possibility of structure in the region between 2 and 3 Bev/c.[11] Such structure would be very important to establish.

The objectives of this experiment were to provide data on the K^+-N total cross sections and the K^+-p differential cross sections at moderately high energies, and to investigate the possible structure in the K^+-p total cross section between 2 and 3 Bev/c.

The experiment was conducted in two phases: First, total cross sections for the K^+-p and K^+-neutron interactions were determined by a conventional beam-transmission method by using a 4-ft-long 6-in.-diam liquid hydrogen (deuterium) target. The same beam and target were then used in conjunction with spark chambers and scintillation counters for the differential cross-section measurements.

In this thesis we will describe the formation of the K^+ beam, in Sec. II. The experimental technique and the results of the total cross-section measurements are described in Sec. III. In Sec. IV the differential cross-section measurements are described. A discussion of the results of the applications of dispersion theory and a phase-shift analysis of the differential cross section is presented in Sec. V. A derivation of the forward dispersion relations for $K^\pm$ proton scattering is presented in Appendix B.

II. THE K^+ BEAM

A. Formation of the Beam

The beam layout is depicted in Fig. 1. Particles were produced by the internal proton beam of the Bevatron striking a 4-× 1/2-×1/4-in. Heavymet target. Those particles emitted at an angle of 26 deg to the internal beam direction and within a solid angle of about 2 msr were focused by the first quadrupole doublet Q_1 at the center of the field lens Q_2. The C magnets M_1 and M_2 steered the beam clear of the Bevatron structure. The beam then passed through the gas Cerenkov counter C_1, the quadrupole field lens Q_2, and the second Cerenkov counter C_2. The field lens Q_2 increased the beam intensity at the hydrogen target by about a factor of 2. The final bending magnet M_3 defined the central momentum of the beam entering the target. The momentum spread was limited by the aperture of the field lens Q_2, and was about ± 4%. The quadrupole Q_3 formed the final image at the T counter for the total cross-section measurements, and at H_3 (subsec. IV-A2) for the differential cross-section measurements. The total path length from production target to the hydrogen target was about 85 ft. The beam size at the T counter was approximately 2 in. in diameter at half-maximum intensity at all momenta above 1.5 Bev/c, and somewhat larger at lower momenta. The largest beam size occurred at 0.8 Bev/c (3 in. diam). The upper limit on the momentum for which the beam could be tuned was set by the C magnets M_1 and M_2, which had to provide the initial bend necessary to get the beam clear of the Bevatron. The lower limit was set by the K-particle flux, which fell of rapidly in the region of 800-Mev/c momentum.

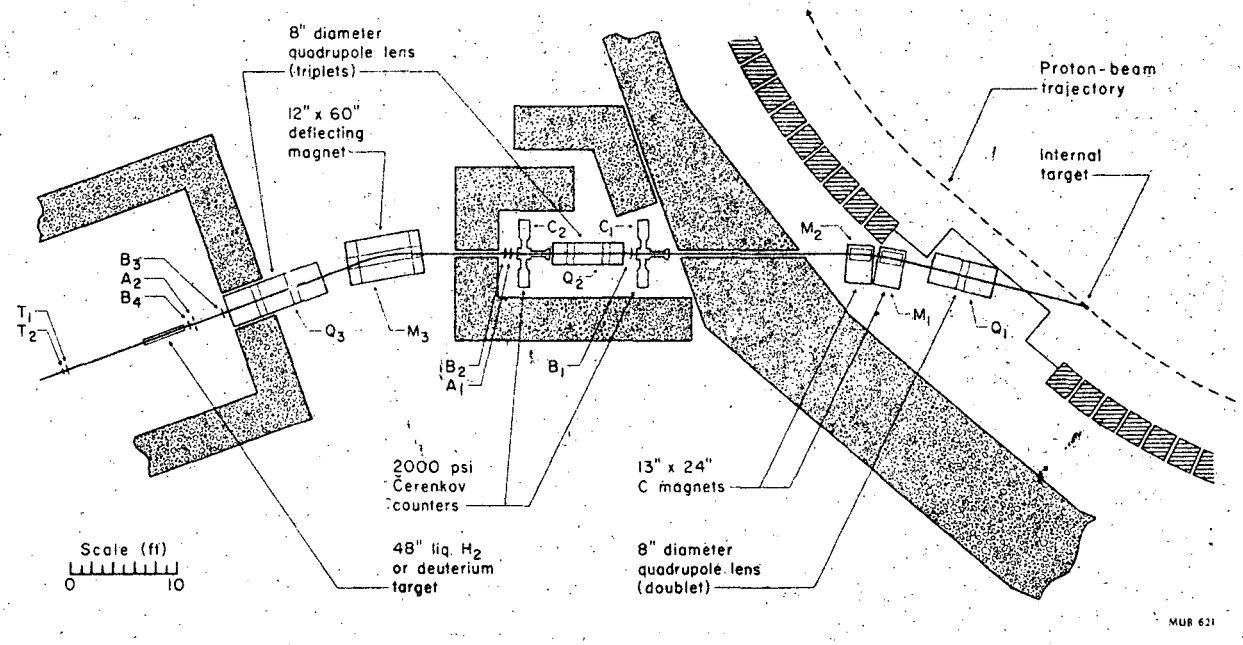

Fig. 1. Beam layout for K^+-N scattering experiment

B. K^+ Particle Selection

The two gas Cerenkov counters (C_1 and C_2) and time-of-flight between the beam-counter pairs B_1, B_3 and B_2, B_4 were used to select particles of K mass from the momentum-analyzed beam. A complete description of the Cerenkov counters is given in reference 12. These counters were designed to detect particles having velocities in either of two velocity intervals. In this experiment the counters were set so that K's and π's of the same momentum were detected. This momentum could be changed by varying the gas (methane) pressure in the counters.

Whenever a K entered the hydrogen target a "K-gate" signal was generated. In addition to the Cerenkov-counter K signals [$C_1(K)$, $C_2(K)$] the K-gate circuitry (Fig. 2) required: that there be no signal from the π channels [$C_1(\pi)$, $C_2(\pi)$]; "yes" signals from the beam defining counters (B_1, B_2, B_3, B_4); no signal from the hydrogen target antidefining counter (A_2); and no signal from the accidental anticounter (A_1).

The large proton flux in the beam was a source of contamination for two reasons. First, δ rays that were produced in the Cerenkov counters could produce light which could simulate the Cerenkov light of K particles. The protons producing the δ rays could then continue on down the beam channel and would be counted as K's. This source of contamination was practically eliminated by the use of two Cerenkov counters, since the probability of having δ rays of the right energy and angle to simulate K's produced in both counters is extremely small.

Protons could also cause accidental coincidence counts because of the high beam flux. Protons which passed down the beam before or after a K particle, and within the resolution time of the K selection circuits, could contribute to the measured transmission rate. This would lead to an erroneously small cross section. The A_1 counter and circuitry were designed to eliminate this source of contamination by providing an output pulse whenever a K was accompanied by a second particle within ± 50 nsec. This pulse was used in anticoincidence in the K-gate circuit.

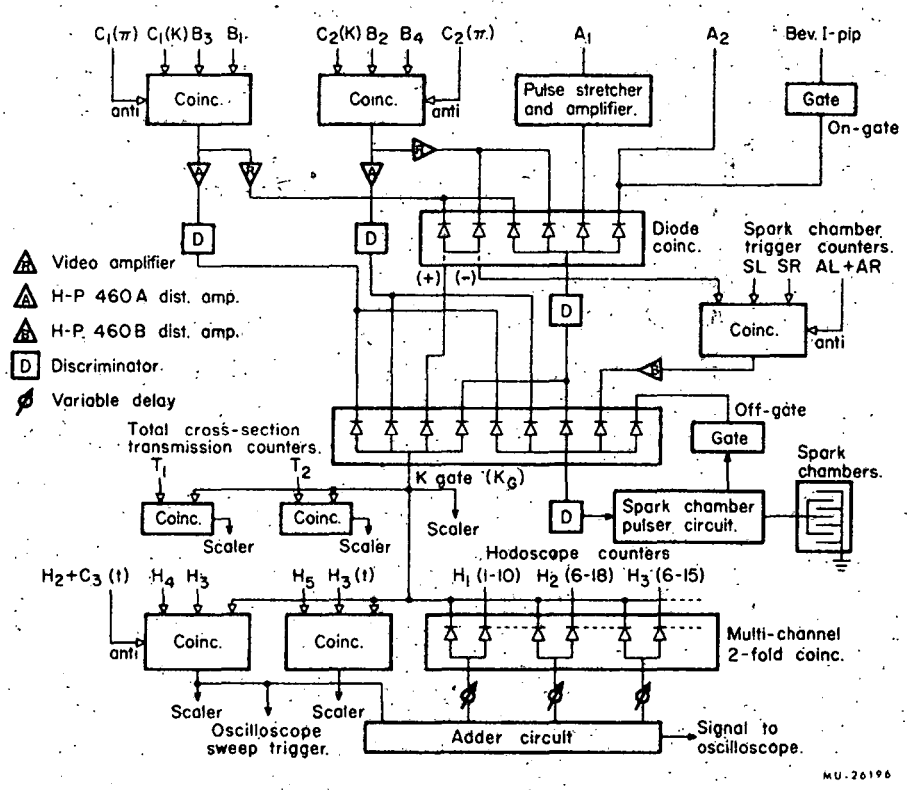

Fig. 2. Simplified block diagram of electronics.

The K-gate can be written symbolically as

$$K_G = C_1(K) + C_2(K) + B_1 + B_2 + B_3 + B_4 - A_1 - A_2 - C_1(\pi) - C_2(\pi) .$$

At low momenta the Cerenkov counters could not be made to count π's and K's separately in the two velocity intervals. At these momenta only the π anti signals were used. Time of flight was used to separate K's and protons.

C. Composition of the Beam

The beam counting rate was measured at each momentum as a function of gas pressure in the two Cerenkov counters. A typical pressure curve is presented in Fig. 3. Similar pressure curves were taken at each momentum to find the optimum operating pressure for K particles, and to measure the abundances of π's and protons in the beam. The measured yields are plotted versus momentum in Fig. 4.

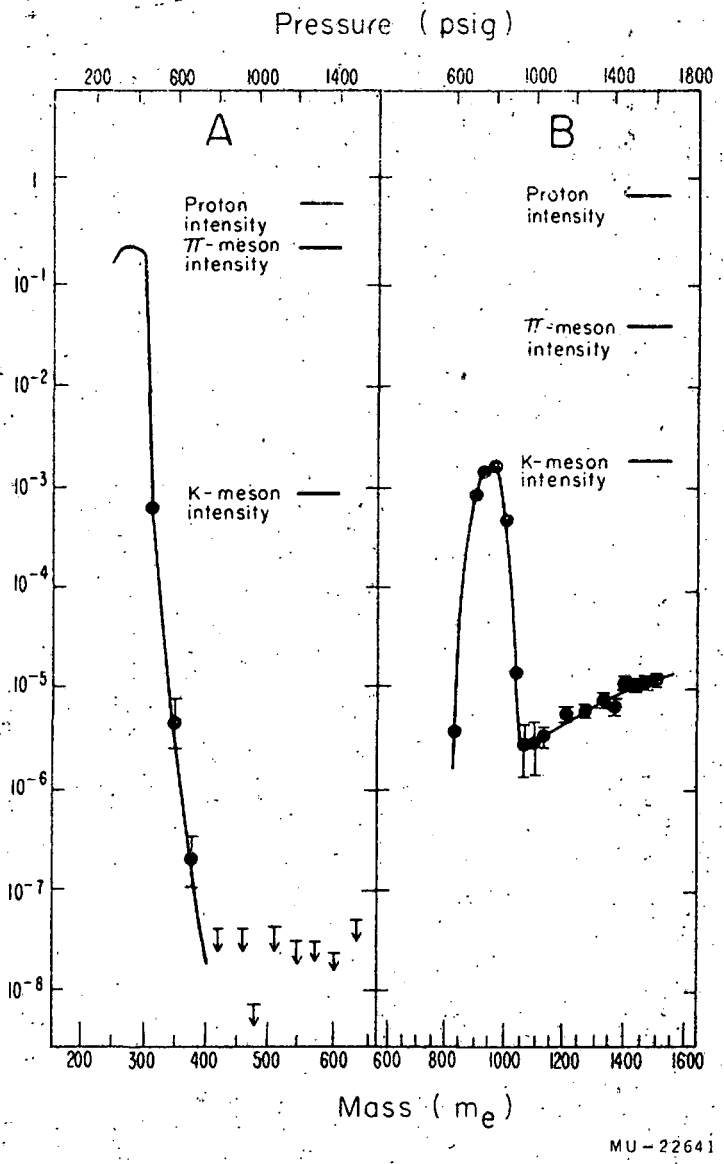

Fig. 3. Coincidence rate in the Cerenkov and scintillation counters normalized to the total flux of particles in the selected beam. (a) Results at 1 Bev/c. At this momentum the Cerenkov counters were used only to anti π mesons. No counts were recorded for any mass selection between 420 m_e and 630 m_e, as indicated by the arrows. The bar at the tail of each arrow indicates the rate if one count had been obtained. (b) Results at 2.3 Bev/c; the background coincidence rate rises with pressure because of proton-induced delta rays.

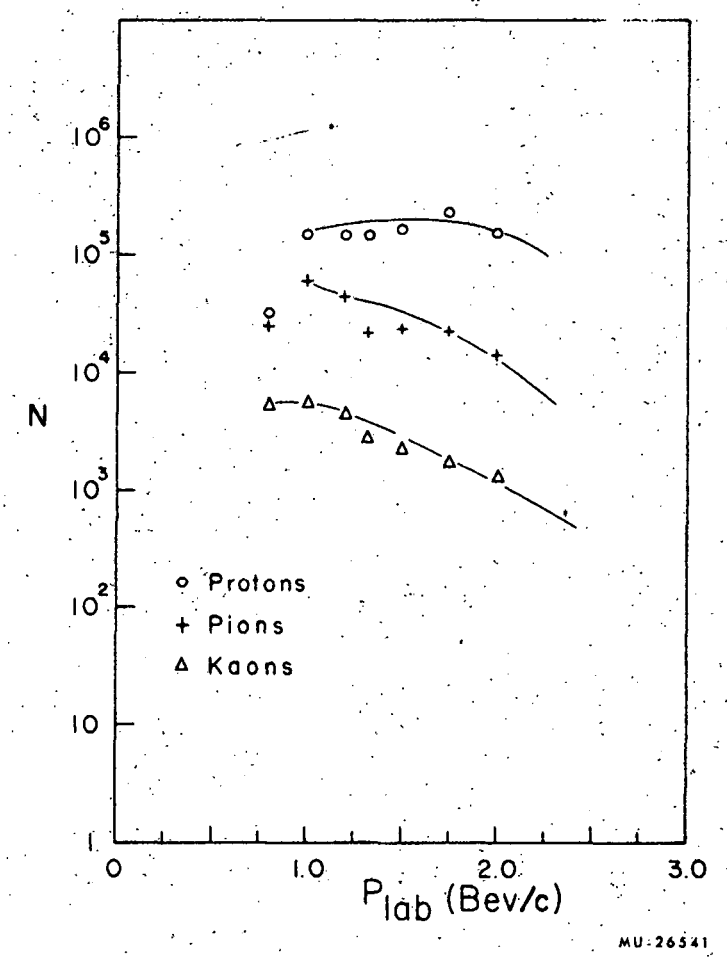

Fig. 4. The composition of the beam stated in terms of the number of particles per 10^{11} protons incident on a 5-in. Heavymet target per 1.5 msr, and for a momentum spread $\Delta p/p = 0.08$. Rates measured at about 90 ft from the production target were corrected for decay in flight and absorption in the Cerenkov counters to deduce the approximate production rates.

III. TOTAL CROSS-SECTION MEASUREMENTS[13]

A. Experimental Method

The total cross sections for K^+-p (σ_d) were determined by measuring the transmission rates of K's through a 4-ft-long 6-in.-diam target, which could be filled with either liquid hydrogen or liquid deuterium. Two transmission counters were used. One of these was a 9-in.-diam circular scintillator (T_1) and the other was a 12-in. square (T_2). Several measurements were made at each energy with the target alternately full and empty.

In terms of the transmission rates with target full (T_F) and empty (T_E), the total cross section is

$$\sigma = \frac{1}{\rho_v L} \ln \frac{T_E}{T_F}, \tag{1}$$

where ρ_v = number of protons in the target per unit volume

L = length of target,

and the statistical error in the cross section is

$$\begin{aligned} \Delta\sigma &= \sqrt{(\partial\sigma/\partial T_E)^2 (\Delta T_E)^2 + (\partial\sigma/\partial T_F)^2 (\Delta T_F)^2} \\ &= \frac{1}{\rho_v L} \sqrt{(\Delta T_E/T_E)^2 + (\Delta T_F/T_F)^2} \\ &= \frac{1}{\rho_v L} \sqrt{\frac{1-T_E}{N_E} + \frac{1-T_F}{N_F}}, \end{aligned} \tag{2}$$

where N_E = number of K's transmitted with target empty,

N_F = number of K's transmitted with target full.

The K^+-neutron cross sections were determined by measuring the K^+-deuterium cross section and making the subtraction

$$\sigma_n = (\sigma_d - \sigma_p)\, g, \tag{3}$$

where g is the correction factor arising from the screening of the neutron.

B. Corrections

The measured cross sections had to be corrected for: (1) decay of K's; (2) forward scattering and forward recoil; (3) multiple scattering in the target; and (4)screening of the neutron by the proton in deuterium, which applied only to the neutron cross sections.

(1) The necessity for the decay-in-flight correction arises chiefly because of the energy loss by the K's in traversing the hydrogen target. With the target full this amounts to about 40 Mev/c in liquid hydrogen. The first-order correction can be easily calculated to reduce the measured cross section by the amount

$$\Delta\sigma^{(1)} = + \frac{d}{\rho_v L} \left(\frac{1}{\lambda_F} - \frac{1}{\lambda_E} \right), \tag{4}$$

where d = distance from the center of the hydrogen target to the T counter,

λ_F = mean free path for decay of a K after traversing half the hydrogen target with target full,

λ_E = mean free path for decay of a K with target empty.

The mean free path for decay can be written

$$\lambda_F = \tau c (\beta\gamma)_F$$

where τ = mean life of K,

c = velocity of light,

$(\beta\gamma)_F = \frac{p_F c}{M_K}$, ($p_F$ is the K momentum with the target Full),

and M_K is the rest energy of the K. Then

$$\lambda_F = \lambda_E + \Delta\lambda$$

and

$$\frac{1}{\lambda_F} - \frac{1}{\lambda_E} = - \frac{\Delta\lambda}{\lambda_E(\lambda_E+\Delta\lambda)} \approx - \frac{\Delta\lambda}{\lambda_E^2} = \frac{\Delta p\, M_K}{p_E^2 c^2 \tau},$$

$$\Delta\sigma^{(1)} = \frac{1}{\rho_v L} \frac{\Delta p\, M_K}{p_E^2 c^2 \tau}. \tag{5}$$

In Eq. (5) we assume that all the hydrogen is concentrated at the center of the target, and we neglect decays upstream from the hydrogen target, and the probability that some decay products will count in the T counter. The exact integrals that must be calculated to evaluate this effect are of the form

$$I = \Sigma f_i \int_{Z_1}^{Z_2} \frac{\Omega_i(Z)\exp[-Z/\Lambda(Z)]}{4\pi} \, dz, \qquad (6)$$

where f_i = branching ratio for ith decay mode,

$\Omega_i(Z)$ = solid angle subtended by the T counter at Z, for the ith decay mode,

$\Lambda(Z)$ = mean free path for the disappearance of a K from the beam, due to scattering and decay.

Integrals of this type were evaluated numerically on an IBM 704 computer.[14] The correction to the first-order decay-in-flight correction was at most 5%.

(2) The forward scattering and forward recoil corrections were estimated by making use of the forward and backward scattering cross sections measured in this experiment at 0.97, 1.17, and 1.97 Bev/c, and interpolating or extrapolating to values for the other momenta. The correction to the measured total cross section is approximately

$$\Delta\sigma = \int_{\theta=0}^{\theta_c} \frac{d\sigma(0)}{d\Omega} \, d\Omega \approx \frac{d\sigma(0)}{d\Omega} \, \Delta\Omega, \qquad (7)$$

where $\Delta\Omega$ equals the solid angle subtended by the T counter at the center of the hydrogen target, and θ_c is the cutoff angle defined by the transmission counter as seen from the center of the hydrogen target.

(3) The correction for multiple Coulomb scattering in the hydrogen target is significant only for beam distributions having transverse (to the beam direction) dimensions of the same order as the transmission counter.

If $n(r)$ is the distribution of beam particles in the radial direction (assumed axially symmetric, which was nearly the case in this experiment), and N_M is the number of particles counted by the T counter with target full, the correction to the total cross section arising from multiple scattering is (see Appendix A)

$$\Delta\sigma = + \frac{1}{\rho_v L N_M} \frac{\langle\theta\rangle^2 d^2}{2} \left.\frac{dn}{dr}\right|_{R_T}, \qquad (8)$$

where ρ_v = number of protons in the target per unit volume

L = length of hydrogen target,

R_T = radius of the T counter,

$\langle\theta\rangle^2 = (15/p\beta)^2 (L/X_0)$ = projected rms scattering angle, where

X_0 = radiation length in hydrogen,

$\left.\frac{dn}{dr}\right|_{R_T}$ = slope of distribution function $n(r)$ evaluated at the radius of the T counter.

The correction is seen to depend upon the size of the T counter. In fact, this effect accounted for nearly all of the difference between the T_1 and T_2 transmission rates at the two momenta where the correction was not completely negligible, i.e., at 0.77 and 0.97 Bev/c.

(4) The neutron-screening correction has been calculated by Glauber.[15] A simple model in which the neutron and proton are considered to be black disks, and the D-wave contribution to the deuteron wave function is neglected, leads to the expression for the K-neutron cross section:

$$\sigma_n = \frac{\sigma_d - \sigma_p}{1 + \frac{\sigma_p}{4\pi}\left\langle\frac{1}{r_d}\right\rangle^2}, \qquad (9)$$

where $\left\langle\frac{1}{r_d}\right\rangle$ is the rms value of the reciprocal of the deuteron radius.

C. Results

The measured total cross sections, with the corrections discussed in Subsec. III-B applied, are presented in Table I. After all corrections had been made there remained a small systematic difference between the cross sections calculated from the T_1 and T_2 transmission rates. The results given in Table I are averages of the corrected cross sections, and may therefore contain a systematic error of —at most— ± 0.3 mb, affecting all values equally. The total cross sections for K_n and K_p are nearly constant and equal over the entire energy range investigated in this experiment. Our K^+-p results in the 2- to 3-Bev/c region fall between the values found by von Dardel et al. and Burrowes et al.,[11] and, as mentioned above, indicate an absence of structure.

A compilation of some recent measurements of K^+-N total cross sections, including ours, is presented in Fig. 5.

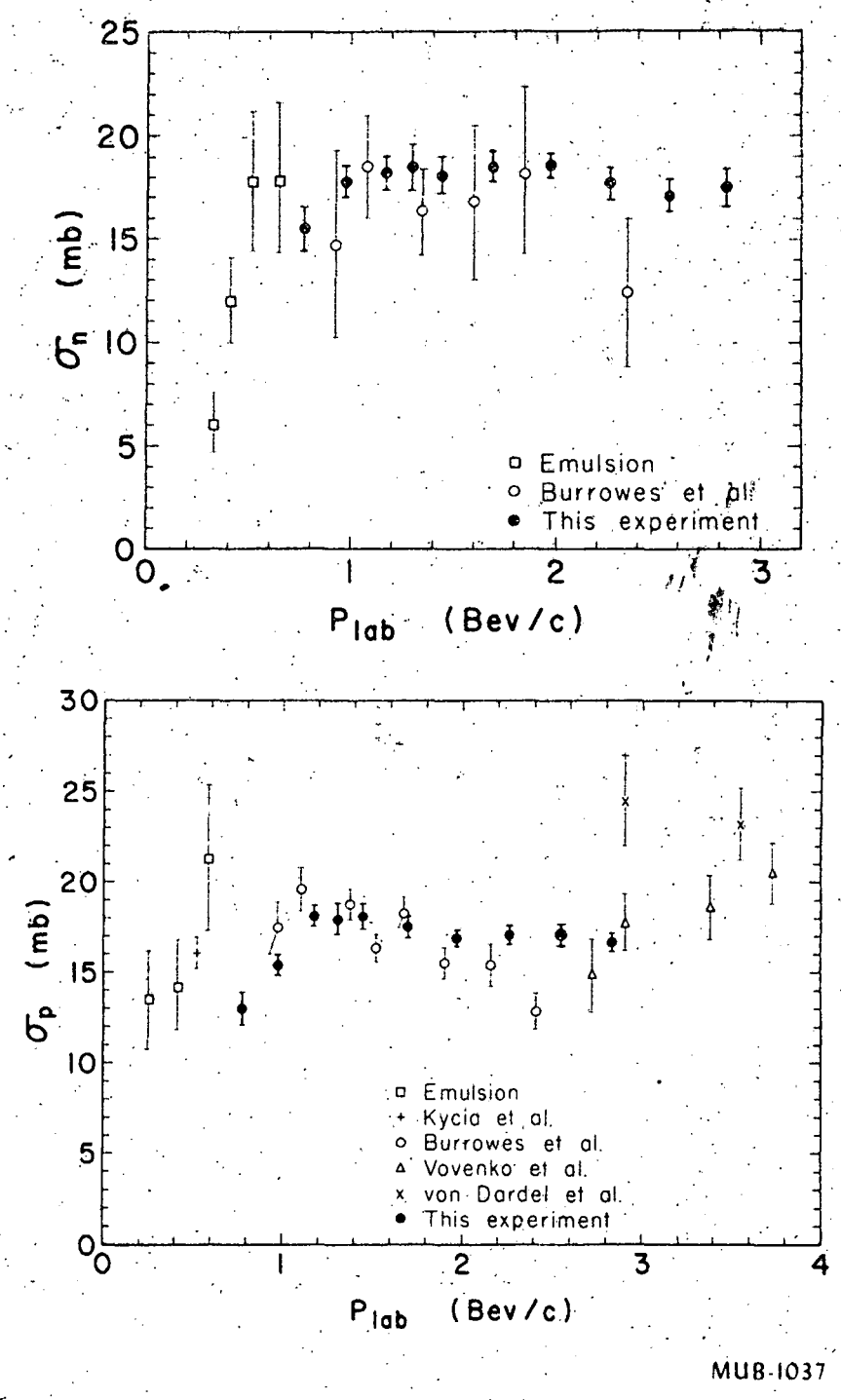

Fig. 5. The K^+-proton (a) and K^+-neutron (b) total cross sections up to 4-Bev/c laboratory momentum.

Table I. Total cross sections: K^+-proton, K^+-deuteron, and K^+-neutron. (Corrections that have been applied are described in Subsec. III-B of the text.)

Momentum (Bev/c) (mb)	0.77	0.97	1.17	1.30	1.44	1.69	1.97	2.26	2.55	2.83
σ_p	13.0 ± 0.0	15.4 ± 0.6	18.1 ± 0.6	17.9 ± 0.9	18.1 ± 0.7	17.5 ± 0.6	16.9 ± 0.4	17.1 ± 0.5	17.1 ± 0.6	16.7 ± 0.5
σ_d	27.3 ± 0.6	32.4 ± 0.5	35.4 ± 0.5	35.6 ± 0.6	35.4 ± 0.5	35.1 ± 0.5	34.6 ± 0.5	33.9 ± 0.6	33.4 ± 0.5	33.4 ± 0.7
σ_n	15.5 ± 1.1	17.8 ± 0.8	18.2 ± 0.8	18.5 ± 1.1	18.1 ± 0.9	18.5 ± 0.8	18.6 ± 0.6	17.7 ± 0.8	17.1 ± 0.8	17.5 ± 0.9

IV. DIFFERENTIAL CROSS SECTIONS

A. Experimental Method

The arrangement of the apparatus used in measuring the differential cross sections is illustrated in Fig. 6. The beam and K^+ selection were the same as in the total cross-section experiment. Spark chambers were used as detectors for K^+-p scatters in the range 15 deg $\lesssim \theta_k, \theta_p \lesssim$ 135 deg (lab angle); a scintillator hodoscope system was used for the range 4 deg $\lesssim \theta_k, \theta_p \lesssim$ 12 deg. The two systems were used simultaneously.

1. The spark chambers. The conducting electrodes of the three identical chambers were made of aluminum-tube frames (1 in. o.d.), over which 0.003-in. aluminum foil was stretched. Thin foil was used so as to keep to a minimum the amount of matter through which the scattered particles passed. There were five such plates per chamber. In addition there were two outer (grounded) plates made of sheets of 0.012-in. aluminum fastened to 1/4-in. flat-aluminum frames. The conducting plates were 10×28 in. and were mounted with 3/8-in. gaps between plates.

The electrode assembly (Fig. 7) was mounted in an aluminum box which could be evacuated, and which was filled to one atmosphere (absolute) of argon during the experiment. The spark discharge could be photographed through a 2-in.-thick Lucite window, which formed one wall of the box. A mirror was mounted in each box to provide a 90-deg stereo view of each electrode assembly.

The three chambers were placed around the hydrogen target as indicated in Fig. 6. A reference grid (scribed on Lucite) was placed directly beneath the hydrogen target. A 5-ft-diam Lucite lens was placed about 10 in. from the spark-chamber windows, with the plane of the lens parallel to the windows, and the axis of the lens passing through the geometrical center of the spark-chamber array. This lens made it possible to photograph sparks that occurred at the end of the spark chamber farthest from the camera.

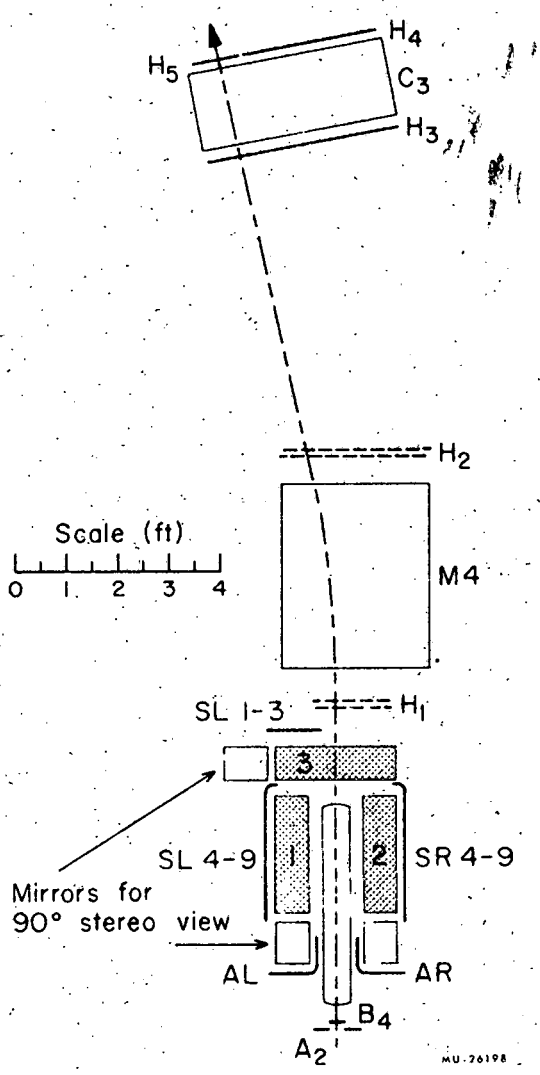

Fig. 6. Spark-chamber and hodoscope counter arrangement for differential cross-section measurements.

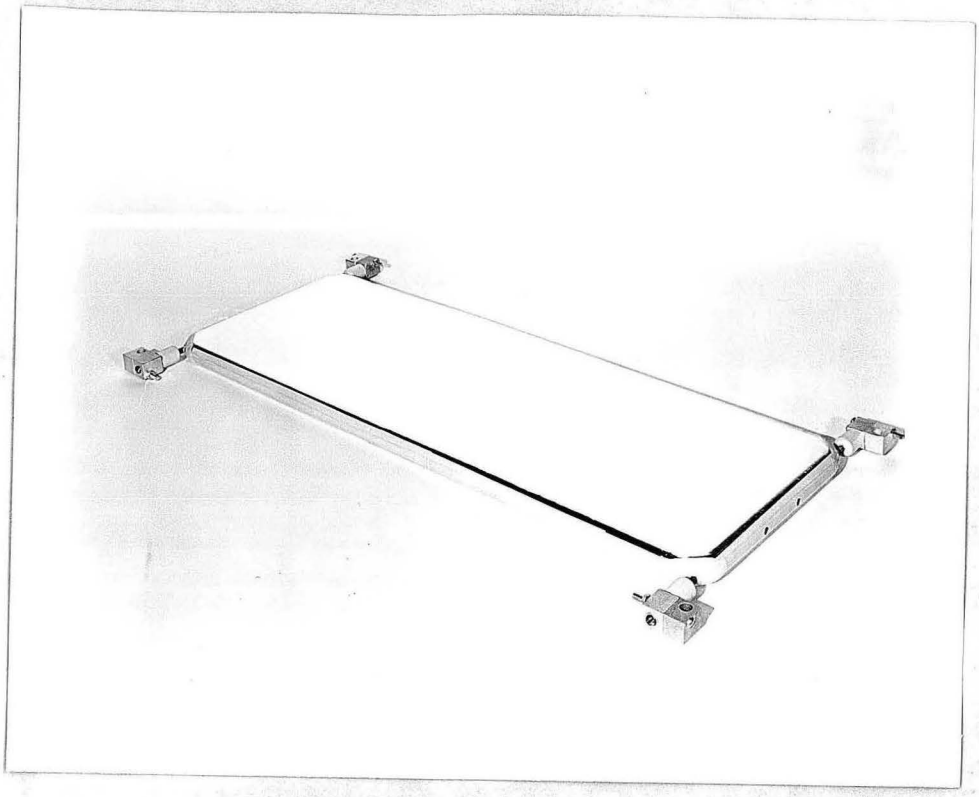

(a)

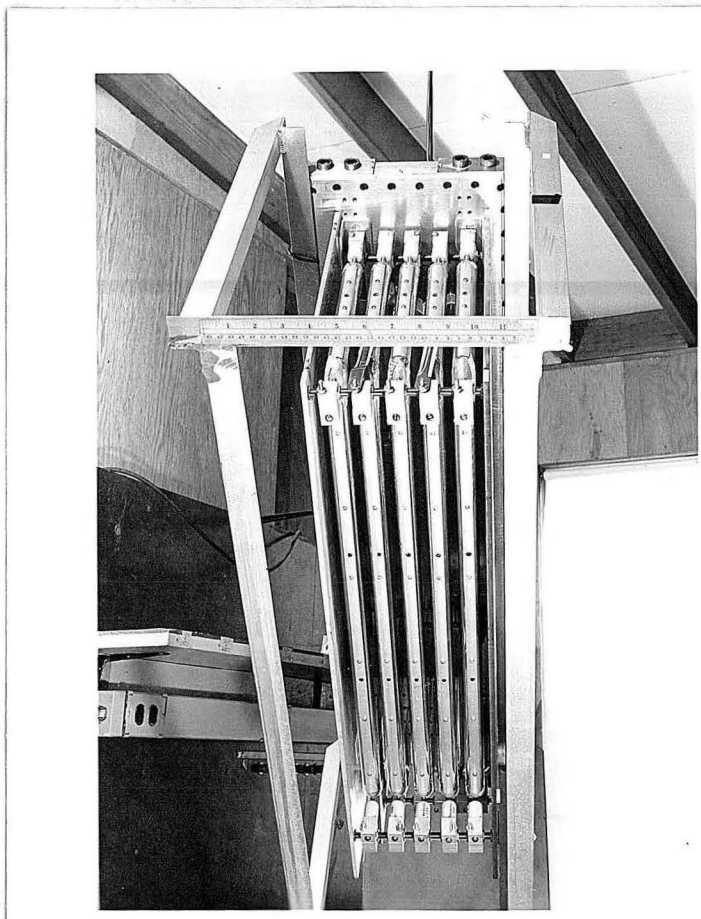

(b)

ZN-3091

Fig. 7. (a). A single aluminum-foil spark-chamber plate.
(b). Spark-chamber plate assembly.

All three of the spark chambers were photographed by a single camera which was placed about 15 ft from the Lucite field lens. Space limitations made it necessary to place one mirror between the camera and the lens.

The number of K's incident on the target was recorded on each frame by placing a K-gate scaler near the spark chamber so that it could be photographed.

The useful volume of the spark chambers was defined by a scintillator array that was mounted flush against the spark-chamber boxes (see Fig. 6). A "K scatter" trigger was generated by a "K-gate" pulse in coincidence with a "left-right" coincidence signal from the SL and SR counters. The K-scatter signal triggered a thyratron circuit (Fig. 8) which provided the negative 20-kv pulse used in generating the spark discharge. The three chambers were connected in parallel and were driven by two hydrogen thyratrons.

A constant positive dc clearing field was applied to the spark-chamber plates to sweep out ions after a discharge, and to shorten the resolving time of the system by sweeping out ions formed by particles passing through the chamber before a K scatter occured. The resolving time of the chambers and electronics was about 500 nsec. About 250 nsec of this time was needed to form the K-scatter signal.

The sparking efficiency is a function of the magnitude of the clearing field, and of the delay time between the passage of the particle through the chamber and the application of the 20-kv pulse to the chamber. In Fig. 9 the sparking efficiency per gap is plotted as a function of delay time for various values of clearing field for each of the three chambers.

Since the cameras which were available at the time were capable of taking only one picture per pulse, the spark-chamber trigger circuit was gated off after each trigger and remained off until the next beam pulse. The same gate was used to turn off the scaler that counted the total number of K's that entered the hydrogen target.

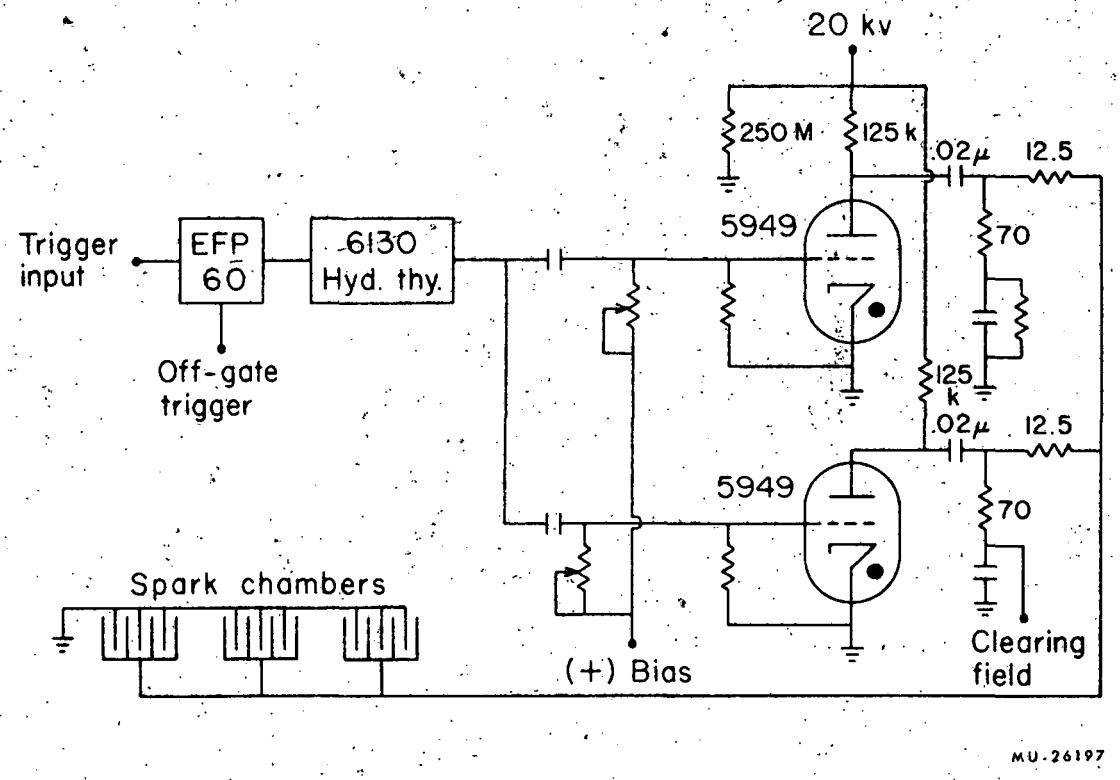

Fig. 8. Spark-chamber pulser circuit.

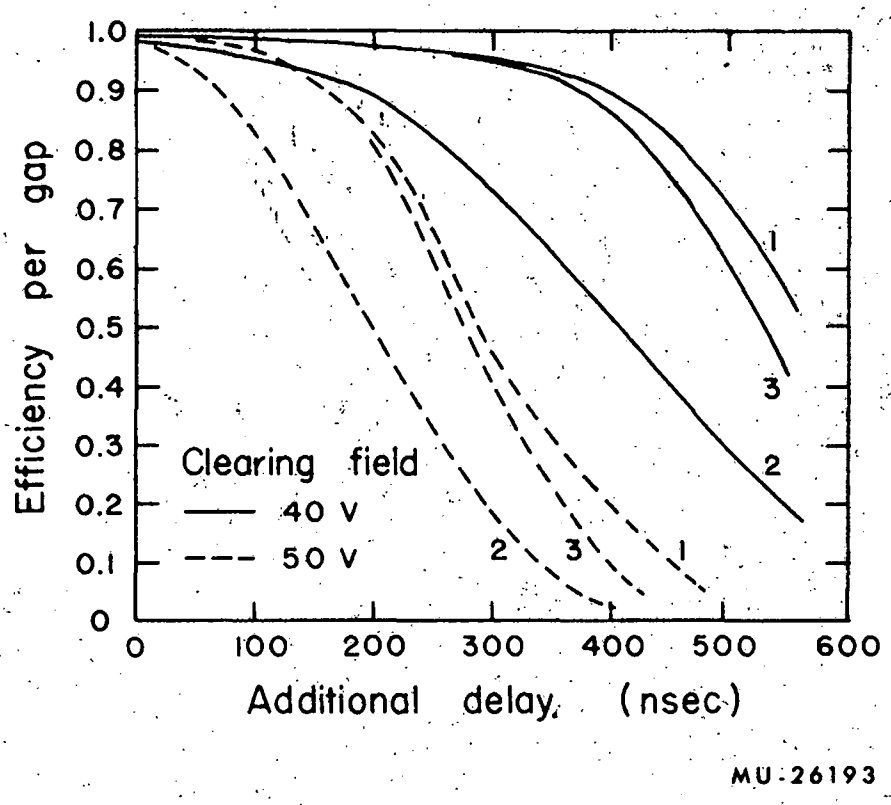

Fig. 9. Spark efficiency per gap as a function of clearing field and time delay between the passage of the charged particle and the application of the high-voltage pulse. Clearing-field polarity (+) is opposite to the polarity of the high-voltage pulse.

2. The hodoscope counter system. The three scintillation-counter arrays H_1, H_2, and H_3 were composed of 10, 18, and 15 counters, respectively. Each scintillator measured 3X8X1/4 in. The H_1 and H_2 arrays were mounted at the entrance and exit ends, respectively, of the bending magnet M_4. Adjacent scintillators overlapped by 1 in. along the 8 in. edge, so that the elements in the x direction (see Fig. 10) were 1X8 in. The H_3 array was placed about 7 ft farther downstream with the scintillators flush along the 8-in. edge, so the elements in the x direction were 3 in.

In the following discussion, and in later sections, we will adopt the following notation. When discussing the individual hodoscope scintillation counters we will write, e.g., H_{11} to refer to the number 1 counter in the H_1 array. When referring to the hodoscope elements we will use the notation $H_1(i)$, etc. The index i runs from 1 to 19, j [H_2 (j)] runs from 1 to 35, and k [H_3(k)] runs from 1 to 15.

Each of the scintillators was viewed by a 6810A photomultiplier. Signals from the photomultipliers were fed to a multichannel two-fold coincidence circuit (Fig. 2), the other input for each channel being the K-gate pulse. Outputs from each channel were applied—through an adder circuit—to the vertical-deflection plates of an oscilloscope. Time delays between the signals were arranged to give the scope presentation illustrated in Fig. 11. The K-gate and the scope trigger pulse were also displayed on the oscilloscope, to provide timing fiducial marks.

The Cerenkov counter C_3 was filled with SF_6 (gaseous) to a pressure of about 250 psi. The pressure was adjusted for a threshold β above that for K's (0.97 at 2.0 Bev/c) and below that for π's with approximately the same momentum as the K's. Thus the combination of the bending magnet M_4 and C_3 (used as an anti-counter) could reject nearly all of the π's and μ's from K decay. The effective radiating volume of C_3 was 48 in. wide, 10 in. high, and about 17 in. deep.[16]

The H_4 scintillator (48X12 in.) ensured that particles accepted as scattered K's (or protons) had passed through C_3. The H_5 scintillator (12X12 in.), placed on the downstream side of C_3 on the beam

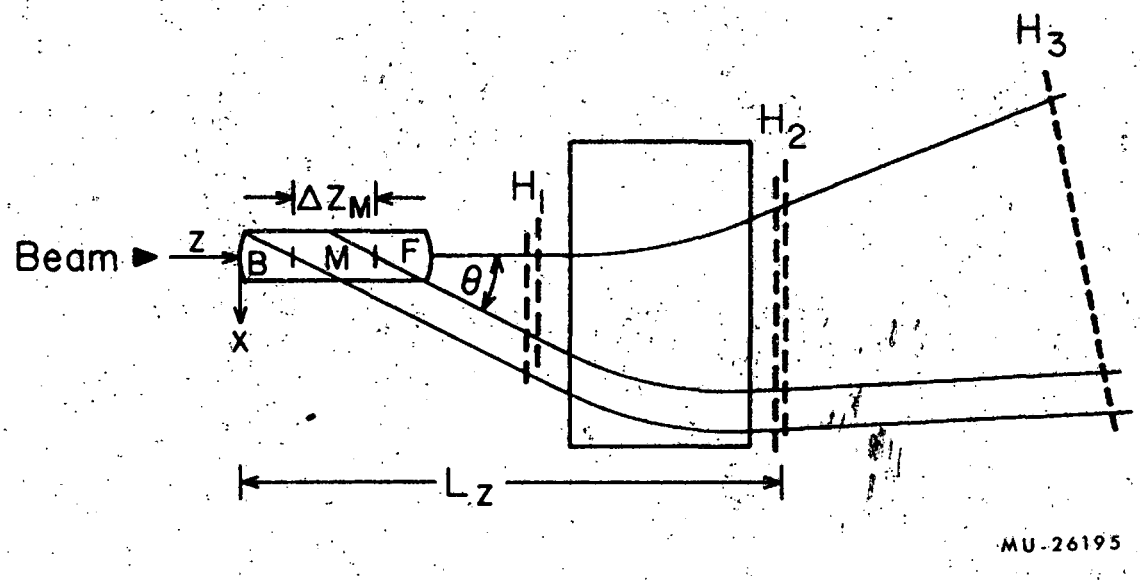

Fig. 10. The hodoscope counter system (compressed by a factor of 2 in the Z dimension) illustrating the definition of the quantities discussed in Subsec. IV-C2.

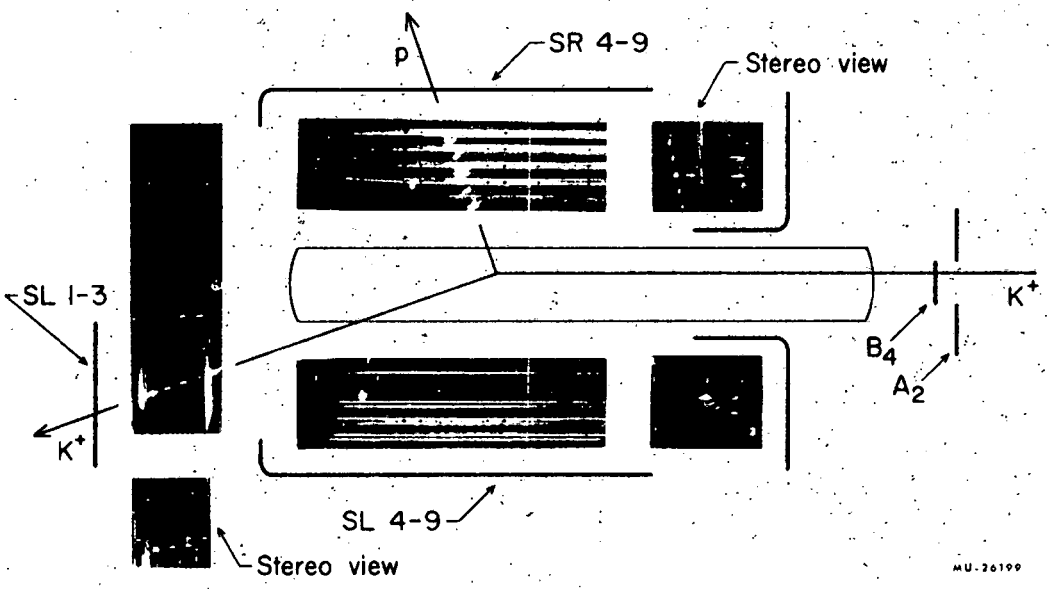

Fig. 11. Format of the oscilloscope trace for the hodoscope data.

center line, measured the transmitted beam. It provided a measure of the beam attenuation by decay in flight, by interactions in the target walls and in the spark chamber (No. 3 was directly athwart the beam), and by C_3. The A_4 counter was composed of four sections that were designed to cover the M_4 pole faces. Its purpose was to reject beam particles that scattered off the pole tips.

The signals from H_{22}, H_{23}, and H_{24} were connected in parallel to form the $H_2(t)$ signal, which was used as an anti to help eliminate beam-particle triggers. The signals from H_{32}, H_{33}, and H_{34} were also connected in parallel to form the $H_3(T)$ signal, which was used in the h_5 coincidence circuit to reduce accidental counts.

The oscilloscope sweep was triggered when the coincidence signal $S_t = K + H_4 + H_3 - H_2(T) - A_4 - C_3$ was generated. The H_3 signal was the sum of the $H_3(k)$ hodoscope counter signals, $H_3 = \sum_{k=6}^{15} H_3(k)$. $H_3(5)$ was disconnected to avoid beam triggers.

For particles of a fixed momentum the angle of scattering was determined by any two of the arrays. The third array could then be used to select particles of a given momentum. Particle trajectories through M_4 were measured as a function of momentum by the wire-orbit technique, and this information was used to determine the elastic-scattering criteria for (i, j, k).

The total solid angle accepted by the detection system was delimited by the H_3 array and, at the center of the hydrogen target, amounted to about 10 msr.

B. Spark-Chamber Data Analysis

1. Film scanning and data reduction. The spark-chamber pictures were scanned on a projection microscope. A typical picture of an elastic K^+-p scatter is presented in Fig. 12. Each picture was assigned to one of the following categories: (1) Good two-prong (opening angle > 70 deg and deviation from coplanarity < 10 deg), (2) Bad two-prong, (3) One-prong, (4) No prongs, and (5) Three or more prongs. The events in the first category were measured by the scanners, who recorded two angles (one in plan and one in elevation view) for each prong, as well as the location of the intersection of the prongs in the two views. All measurements were made with respect to the grid lines, which were parallel (and normal) to the central beam trajectory. The number of incident K's and the number of sparks in each prong were also recorded. All data were recorded directly on IBM punched cards.

A computer program was written that carried out the rather simple logic and algebra required to compare each event with the elastic-scattering criteria. The deviation from coplanarity ($\Delta\phi$) and the deviation from the elastic-scattering-angle curve ($\Delta\theta$) were computed for each event.

For side-side events (prongs in chambers 1 and 2), $\Delta\phi$ was simply the angle between the two prongs in the elevation view. For front-side events (prongs in chambers 1 or 2, and in chamber 3), a simple calculation was required to determine $\Delta\phi$.

A typical plot of the larger angle (θ_L) against the smaller angle (θ_S) for elastic K^+-p scattering is given in Fig. 13. The angles measured for each event $[\theta_L(M), \theta_S(M)]$ correspond to a point on this plot. The deviation $\Delta\theta$ was defined as the normal distance from $[\theta_L(M), \theta_S(M)]$ to the curve. For events which fell between the two branches of the curve both $\Delta\theta$'s were calculated, and the event was assigned to the branch resulting in the smaller $\Delta\theta$. The "true" scattering angles for the event were taken to be those at the intersection of the curve and the normal from $[\theta_L(M), \theta_S(M)]$. The cosine of the "true" K scattering angle in the c.m. was calculated by the computer.

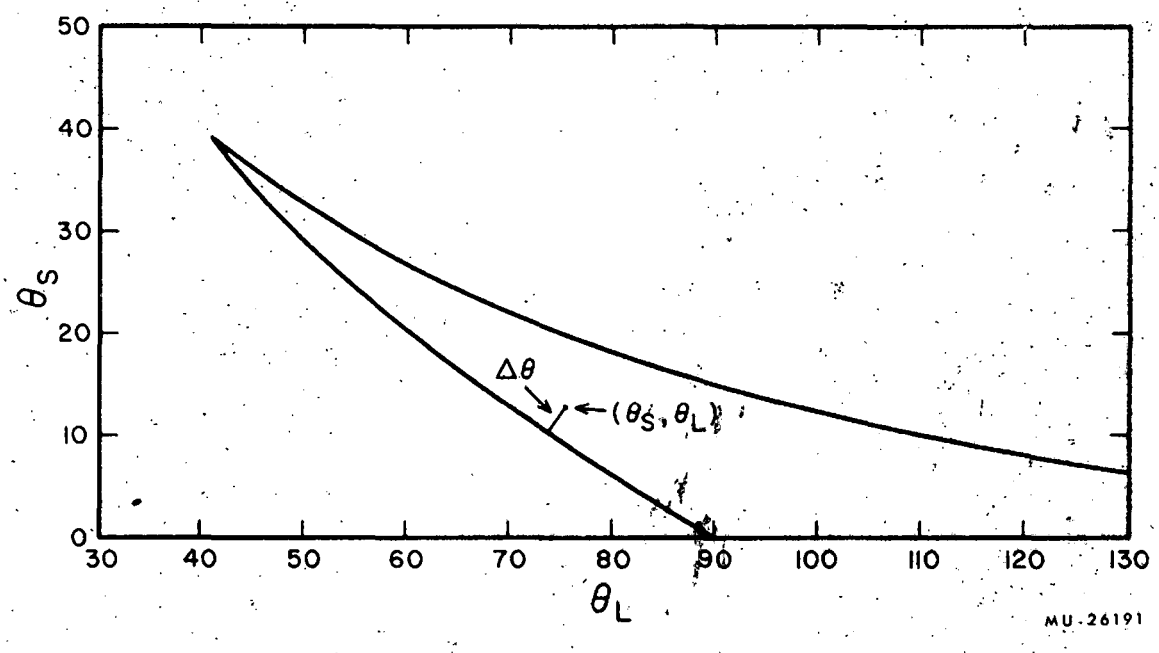

Fig. 12. Spark-chamber picture of a K^+-p elastic scatter. Incident K^+ momentum is 1.2 Bev/c.

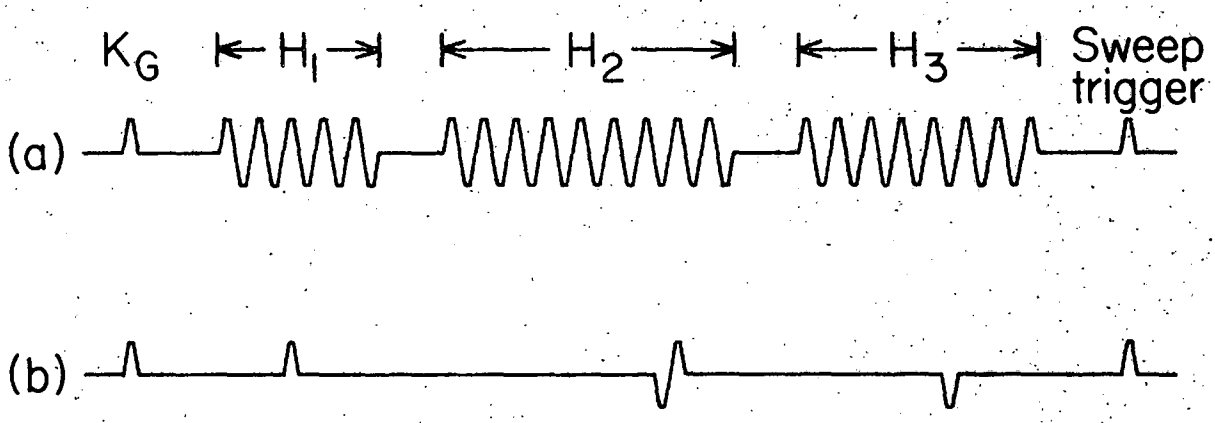

Fig. 13. Plot of the smaller angle θ_S against the larger angle θ_L for elastic K^+-p scattering.

Cutoffs for $\Delta\theta$ and $\Delta\phi$ for acceptable (elastic) events were determined by examining the distributions in $\Delta\theta$ and $\Delta\phi$, which peaked up sharply about $\Delta\theta$, $\Delta\phi = 0$, and then setting the cutoffs at the point where the distributions fell to the background level outside the peaks. The validity of the cutoffs in $\Delta\theta$ and $\Delta\phi$ was checked by varying the cutoff slightly, and requiring that the results should not be significantly changed. The cutoffs were largest for forward and backward scattering, which is to be expected for two reasons:

(a) Multiple scattering in the hydrogen and aluminum of the target for low-energy recoil protons (forward scattering) and K's (backward scattering) becomes appreciable in these regions. At 1.17 Bev/c this amounted to about 1 deg in the forward scattering region, and about 1.7 deg in the backward scattering region.

(b) Angular divergence of the incident beam could result in a large spread in $\Delta\phi$ for the two extremes of the angular range. Values for $\Delta\theta$ and $\Delta\phi$ were calculated under the assumption that the incident particle was moving parallel to the beam axis. If the angle between the incident K direction and the beam was 2 deg, the observed noncoplanarity for an elastic scatter could be as large as 8 deg for the extremes of the angular range.

The estimated uncertainty in the number of elastic scatters due to the arbitrary cutoffs in $\Delta\theta$ and $\Delta\phi$ is less than 2% at most angles. In the extreme forward and backward directions the results were more sensitive to the selection of the cutoffs, the estimated uncertainty being about 5% for these regions.

The contamination of inelastic scatters in the accepted elastic events was estimated by determining the density of rejected 2-prong events in the $(\Delta\theta, \Delta\phi)$ plane, outside the $(\Delta\theta, \Delta\phi)$ cutoff region. The correction was made assuming that these events were uniformly distributed throughout the $(\Delta\theta, \Delta\phi)$ plane.

Measurement accuracy was found to range from 0.5 to 1 deg, the greatest accuracy being achieved for particle trajectories normal to the spark-chamber plates.

The momentum spread ($\Delta p/p \approx \pm 0.04$) and the angular divergence of the incident beam (about $\pm$ 1 deg) introduced an uncertainty in the expected elastic-scattering kinematics that was estimated to be about ± 1.5 deg. This uncertainty combined with the measurement error could account for a width in the $\Delta\theta$ distribution for elastic scatters of from about 3 (± 1.5) to 5 deg.

All events which on the initial scan were assigned to category 5 (three or more prongs) were rescanned and checked against the hypothesis that two of the prongs comprised an elastic scatter whereas the others were accidentals. About 15% of this group were found to fit this hypothesis. Most of them were a result of either beam-particle accidentals which could enter the fiducial volume of the spark chamber 3 because of the width of the beam, or proton scatters in the target.

2. Differential cross section. The differential cross section in the c.m. system can be written

$$\frac{d\sigma}{d\Omega}_i = \frac{N_i \epsilon_i a_i \beta_i}{n_p n_K \Delta Z_i \Delta\phi_i (\Delta\cos\theta)_i} ,$$

where

N_i = number of elastic scatters found in the ith interval of $\cos\theta$,
n_p = number of protons in the target per unit length,
n_K = number of K's incident on the hydrogen target,
ΔZ_i = effective target length for the ith interval,
$\Delta\phi_i$ = effective azimuthal angular range accepted by the spark chambers,
ϵ_i = correction for protons stopped in the hydrogen, in the walls of the target, and in the spark chambers,
a_i = correction for loss of K particles due to scattering and decay in flight,
β_i = correction for loss of protons due to scattering,
θ = c.m. scattering angle of the K.

The effective length of the hydrogen target (ΔZ) as a function of scattering angle and of x and y, was calculated from the known geometry of the detection system. The ΔZ_i were evaluated approximately by weighting the calculated values $\Delta Z\ (x, y, \cos\theta)$ according to the measured beam distribution, and then averaging over the $\Delta \cos\theta$ interval.

The azimuthal angular range ($\Delta\phi$, measured in the x-y plane) accepted by the spark chambers is a function of x, y, Z, and $\cos\theta$. The $\Delta\phi\ (x, y, Z, \cos\theta)$ could be calculated from the geometry of the system. The $\Delta\phi_i$ is an average over $(\Delta \cos\theta)_i$ of the $\Delta\phi$ weighted according to the beam distribution.

3. Corrections. The low-energy recoil protons from small-angle K scatters could be stopped in the hydrogen or in the walls of the target or spark chambers. This effect reduces the number of small-angle K scatters that are detectable. The correction ϵ_i depends upon the beam distribution and the scattering angle. The $(\cos\theta)_i$ intervals were chosen so that ϵ_i is appreciable only in the interval nearest $\cos\theta = +1$.

The K decay and interaction loss (α) and the proton interaction loss (β) were calculated as functions of x, y, Z, and θ, and then averaged for each $\Delta\cos\theta_i$.

C. Hodoscope Data Analysis

1. Scanning and data reduction. The format of the hodoscope film traces is illustrated in Fig. 11. Each trace was scanned and designated as one of the following types:

a. Good traces. The K-gate (G) and the scope-trigger (T) pulses were required. In addition there could be no more than two "scatters" indicated by the pulses from each hodoscope array.

b. Spark traces (with G). Radiation from spark-chamber discharges was picked up by the hodoscope electronics and the oscilloscope, usually resulting in a spurious scope trace with the large noise pulse from the spark discharge clearly evident on the trace. Occasionally the spark chambers and the hodoscope system were triggered by the same

particle. The resulting traces contained a G pulse followed, after a characteristic time delay, by the spark-chamber noise pulse. A correction for such events (spark traces with G) had to be made, since they represented a possible loss of good scatters.

c. Blank traces.

d. Traces indicating more than two scattered particles in any of the three hodoscope arrays.

e. Unreadable traces.

The pulses present on type(a) traces were recorded on IBM cards. A computer program was written to sort these events into: (1) one-particle events, (2) two-particle events, (3) pulses from any one of the arrays missing, and (4) doubtful events. The one-particle events were further sorted into bins designated by (i-j), where the indices refer to the element in which the pulse occurred in the arrays $H_1(i)$, $H_2(j)$, and $H_3(k)$.

In the analysis of the data the first two arrays were used to determine the angle of scattering (proportional to i-j), and the third array was used to select elastic scatters. The elements in $H_1(i)$ and $H_2(j)$ were 1×8 in., and any combination (i-j) determined the scattering angle to about ±1 deg.

The allowed elastic-scattering region in $H_3(k)$ for a given (i, j) combination was, in general, larger than one element (3 in.). Cutoffs in $H_3(k)$ were established by plotting the observed k distribution for each (i, j) combination. These distributions were found to peak around a particular k element for each (i, j); this was designated the elastic scattering element k_e. All events in the bins $(i, j, k_e \pm \Delta k)$ were accepted as elastic scatters. The data were tested for sensitivity to the selection of the cutoffs (Δk) in $H_3(k)$ by varying Δk. In all cases where sufficient data existed to make statistically significant tests possible, the results were found to be insensitive to changes of one element size (3 in.) in Δk. The net number of particles in each bin N(i, j, k) was determined by making a target Full-Empty subtraction.

The events in categories other than "one particle" events were checked for hydrogen scatters; however, all of them disappeared after

the Full-Empty subtraction except in the "two-particle event" and "doubtful pulse" categories.

The two-particle events were tested for a fit to the hypothesis that one particle was an elastic scatter and the other was in accidental coincidence with the K-gate. All possible combinations (i, j, k) fitting this hypothesis were constructed from the pulses found in the two-particle event, and each combination was assigned a weight based on the frequency of its occurrence in the one-particle type events. The weights corresponding to elastic scatters were then added to the total number of elastic scatters.

When the scanners found a pulse which did not meet the pulse-height requirement but appeared to be larger than the usual feed-through pulse size, they were instructed to record it as doubtful. When a particular counter was found to produce "doubtful pulses" frequently, the population of "one particle" events (i, j, k) involving this counter was compared with neighboring combinations. When the "sick" counter combinations were underpopulated the doubtful pulses from that counter were accepted as real, and these "doubtful" events were checked for acceptable elastic scatters.

2. Differential cross section. Consider first the case where all scatters occur on the axis of the hydrogen target. The elastically scattered K's that pass through the hodoscope combination (i, j, k) must have interacted with a proton somewhere in the region ΔZ (refer to Fig. 10). The number of K particles which scatter in ΔZ into (i, j, k) and reach the H_4 trigger counter before decaying or undergoing a second interaction is given by

$$N(i,j,k) \equiv N(a) = \int_{\Delta Z_a} n_K \frac{\overline{d\sigma}(a)}{d\Omega} n_p \Delta\Omega(a, Z) F(a, Z) dZ, \qquad (11)$$

where

n_K = number of K's incident on the hydrogen target,

n_p = number of protons in the target per unit length,

$\frac{\overline{d\sigma}(a)}{d\Omega}$ = K^+-p differential cross section averaged over the angular interval accepted by the ath counter combination,

$\Delta\Omega(a, Z)$ = solid angle subtended by the ath hodoscope combination,

$F(a, Z)$ = correction factor for K attenuation in the hydrogen target, walls of the hydrogen target and the Cerenkov counter C_3, and decay in flight between B_4 and H_4.

The solid angle $\Delta\Omega(a, Z)$ can be written

$$\Delta\Omega(a, Z) \approx \sin\theta_a \, \Delta\theta_a(Z) \, \Delta_a(Z) \, ,$$

where θ_a is the central scattering angle accepted by the ath hodoscope combination. The azimuthal angular range accepted by the hodoscope system was limited by the H_3 array. Since the distance from the target to H_3 ($\gtrsim$150 in.) was large compared to the height of the hodoscope elements (8 in.), we can write

$$\Delta\phi_a \approx \frac{h \cot\theta_a}{Z_3 - \bar{Z}} \, ,$$

where

Z_3 = distance from the entrance end of the hydrogen target to H_3,

h = height of hodoscope elements.

The decay and interaction correction is of the form

$$F(a, Z) = \exp\left[- \sum_m \frac{\ell(a, Z)_m}{\lambda_m} \right] ,$$

where

$\ell(a, Z)_m$ = the path length in the mth medium (hydrogen, aluminum, etc.),

λ_m = mean free path for attenuation due to scattering, absorption, and decay in flight.

The total path length between B_4 and H_4 was about 220 in. The total interval ΔZ was at most about 15 in. If we take $\bar{Z}$ at the center of the interval ΔZ we can write

$$N(a) \approx \frac{n_p n_K h \cos\theta_a}{Z_3 - \bar{Z}} \frac{\overline{d\sigma}(a)}{d\Omega} \quad F(a, \bar{Z}) \int_{\Delta Z_a} \Delta\theta_a(Z) dZ, \qquad (12)$$

which is accurate to about 3%.

Now we must take account of the fact that the K beam is not confined to the target axis. Consider a radially symmetric beam (this was the case, to good approximation, in this experiment). Let x be the coordinate normal to the beam line, as shown in Fig. 10. Then Eq. 12 should be written

$$N(a) = n_p \frac{\overline{d\sigma}(a)}{d\Omega} \frac{h \cos\theta_a}{Z_3 - \bar{Z}} \int_{\Delta Z_a} \int_{-a}^{a} n_K(x) \Delta\theta_a(x, Z) F(a, \bar{Z}, x) dx dZ,$$

where $n_K(x)$ is the beam distribution in x, and $\pm a \approx 2.3$ in. are the limits set by the hydrogen target defining counter B_4. For a symmetric beam the effect on $\Delta\theta_a(x, Z)$ cancels to first order in $\frac{a}{L_2}$ ($\lesssim \frac{1}{30}$), where L_2 is the distance from Z to the hodoscope element $H_2(j)$. Moving off-axis affects only the path length in hydrogen in $F(a, \bar{Z}, x)$, and to first order in $\frac{a'}{L_H}$ ($\lesssim \frac{1}{10}$), where L_H is the path length in hydrogen along the center line, this effect also cancels. This approximation is good to about 2%. These cancellations occur provided the entire beam (symmetric) is sampled at the point Z. This is true for the middle section of the target (labeled M in Fig. 10) but not for the end sections F and B. For the end sections the average beam-particle location (where the cancellations mentioned above do occur) is not on the target axis. There does exist such a point, however, and we can write for the three target regions,

$$N(a) = \frac{n_p n_K h \cos\theta_a}{Z_3 - \bar{Z}} \frac{\overline{d\sigma}(a)}{d\Omega} F_t(a, \bar{Z}) \left[\int_{\Delta Z_a} \Delta\theta_a(Z) dZ \right]_t, \qquad (14)$$

where t takes on the values t = M, F, B.

The expression for the differential cross section as a function of scattering angle can now be written as a sum over the hodoscope combinations a, subject to the constraint i-j = gθ, where g depends on the geometry of the hodoscope system and the angle of deflection in M_4. We have

$$\overline{\frac{d\sigma(\theta)}{d\Omega}} = \frac{\sum_a N(a)}{n_p n_K h \sum_a \cos\theta_a F_t(a, \bar{Z})\, I_t(a)(Z_3 - \bar{Z})}; \qquad (15)$$

$$I_t(a) = \left[\int_{\Delta Z_a} \Delta\theta_a(Z)dZ\right]_t .$$

The integrals I(a) were evaluated by numerical integration for each hodoscope combination a.

The H_5 counting rate (H_5/n_K) (see Subsec. IV-A2) measured the attenuation of the beam by: (1) interaction in the hydrogen target, in the spark chamber walls, and in the Cerenkov counter C_3, and (2) decay in flight between B_4 and H_5. The difference between H_5/n_K and $F(a, \bar{Z})$ is a function of the scattering angle and the geometry of the system.

The net number of counts in each a was arrived at by making the subtraction

$$N_a = N_a(\text{Full}) - \epsilon_a N_a(\text{Empty}),$$

where ϵ_a corrected the empty data for the difference between target Full and Empty attenuation rates.

3. Corrections. Cross sections calculated from (15) were corrected for: (a) proton contamination and (b) vertical focusing in M_4:

a. Proton recoils in the forward direction could not be distinguished from K's. The difference in momentum between protons and K's scattered at small angles was not large enough to be detected by the hodoscope system. Thus the number of scatters detected at an angle θ, N(θ), composed of K's and recoil protons, can be written

$$N(\theta) = N_K(\theta) + N_p(\theta) = N_K(\theta)\left[1 + f\frac{\frac{d\sigma}{d\Omega}(\theta_p=\theta)}{\frac{d\sigma}{d\Omega}(\theta_K=\theta)}\right], \quad (16)$$

where f takes account of the difference in attenuation for K's and protons between the point of scattering and H_4.

b. Vertical focusing in M_4 increased the effective solid angle of the system. The correction was calculated by treating the entrance and exit planes of M_4 as thin lenses with focal length given by

$$F = \frac{\rho}{\tan\theta}, \quad (17)$$

where ρ = radius of curvature in M_4, and θ is the angle between the particle trajectory and the boundary line of the magnetic field region.

D. Results

1. Spark-chamber data. The results of the film scan are presented in Table II. The number of pictures found of each type with target Full and Empty is given, along with the total number of elastic scatters and the number of incident K's (N_K) at each of the momenta investigated. Types 1 and 5 contained all of the elastic scatters. Events in the other categories were inelastic hydrogen scatters, and interactions in the target walls and spark-chamber boxes.

The calculated differential cross sections are given in Table III. The quoted errors include the statistical errors $\sqrt{N(\theta)}$ and estimated systematic uncertainties (7 to 10%). In the film scan, events having $\Delta\phi > 10$ deg were rejected. This rejection was possible, however, only for side-side events. Coplanarity for front-side events could not be checked directly, and was not applied to these events. Since all events in the extreme forward and extreme backward directions were front-side events, no elastic scatters should have been lost because of the $\Delta\phi$ scanning criterion.

Table II. Film-scanning results. ("Types" are discussed in Subsec. B.)

Type	Momentum (Bev/c) 0.97			1.17			1.97		
	Full	Empty	Net[a]	Full	Empty	Net[a]	Full	Empty	Net[a]
1	1214	10	1164	1946	14	1902	1694	17	1625
2	649	66	321	1055	131	744	3166	476	1477
3	960	106	435	1734	212	1068	3340	517	1449
4	212	65	-100	343	68	129	893	234	39
5	671	37	487	638	22	568	2670	212	1881
Total	3706	284	2307	5766	447	4411	11 783	1456	6471
Elastic	1261	0		1699	0		1593	1	
N_K	0.7962 $\times 10^6$	0.1606 $\times 10^6$		1.133 $\times 10^6$	0.3602 $\times 10^6$		2.582 $\times 10^6$	0.5929 $\times 10^6$	

[a] Empty numbers have been normalized to the total number of K^+ (N_K) incident on the Full target.

Table III. Differential cross-sections in K^+-p c.m. system.

Momentum (Bev/c) 0.97			1.17			1.97		
$\cos\theta^*$	$\frac{d\sigma}{d\Omega}$(mb/sr)	$\Delta\sigma_{com}$ [a]	$\cos\theta^*$	$\frac{d\sigma}{d\Omega}$ (mb/sr)	$\Delta\sigma_{com}$ [a]	$\cos\theta^*$	$\frac{d\sigma}{d\Omega}$(mb/sr)	$\Delta\sigma_{com}$ [a]
0.76±0.06	1.07±0.18	0.53	0.78±0.08	1.89±0.24	1.09	0.92±0.02	1.52±0.21	0.69
0.6 ±0.10	0.84±0.09	0.22	0.65±0.05	1.26±0.14	0.32	0.85±0.05	1.84±0.15	0.39
0.4 ±0.10	1.15±0.11	0.27	0.55±0.05	1.19±0.12	0.33	0.75±0.05	1.47±0.14	0.31
0.15±0.15	0.75±0.07	0.17	0.45±0.05	0.95±0.10	0.21	0.65±0.05	1.04±0.11	0.22
-0.1 ±0.10	0.57±0.06	0.13	0.35±0.05	1.04±0.10	0.30	0.55±0.05	0.49±0.06	0.09
-0.3 ±0.10	0.67±0.08	0.17	0.15±0.15	0.61±0.05	0.14	0.45±0.05	0.44±0.06	0.08
-0.5 ±0.10	0.76±0.10	0.22	-0.05±0.05	0.42±0.05	0.09	0.35±0.05	0.32±0.05	0.06
-0.7 ±0.10	0.67±0.09	0.21	-0.15±0.05	0.35±0.05	0.08	0.25±0.05	0.27±0.04	0.05
-0.88±0.08	0.61±0.11	0.27	-0.25±0.05	0.33±0.05	0.08	0.10±0.10	0.12±0.06	0.02
			-0.35±0.05	0.36±0.06	0.08	-0.05±0.05	0.061±0.023	0.011
			-0.45±0.05	0.43±0.07	0.12	-0.15±0.05	0.083±0.028	0.016
			-0.55±0.05	0.24±0.05	0.07	-0.25±0.05	0.056±0.021	0.011
			-0.65±0.05	0.41±0.07	0.13	-0.35±0.05	0.029±0.014	0.006
			-0.75±0.05	0.36±0.06	0.11	-0.45±0.05	0.048±0.016	0.011
			-0.85±0.05	0.43±0.07	0.14	-0.55±0.05	0.054±0.016	0.013
			-0.93±0.03	0.73±0.17	0.28	-0.65±0.05	0.064±0.017	0.015
						-0.75±0.05	0.062±0.017	0.016
						-0.85±0.05	0.081±0.019	0.021
						-0.94±0.04	0.043±0.021	0.013

[a] The listed cross sections include this correction, which is the sum of the corrections for stopping proton loss, proton interaction, and K decay and interaction.

2. Hodoscope data. The results of the hodoscope film scan are summarized in Table IV. Of the total number of sweeps photographed about 50% were triggered by the spark chambers, 35% were analyzed for elastic scatters, and the remaining 15% were of the following types (approximate percentage in parentheses).

a. H_2 missing (7%). There were no "net hydrogen" events of this type after the target Full-Empty subtraction. This implies that they are most likely unscattered beam particles which do not provide an anti pulse in $H_2(T)$, or decays in flight which manage to miss H_2.

b. Blank (3%). No K-gate or sweep trigger (T) were visible on the sweep. These were accidental scope triggers which introduce no uncertainty in the results.

c. H_3 missing (1%). These were due to (i), the loss of signal from one or more of the H_3 counters between the counters and the oscilloscope, or (ii), accidental scope triggers, since H_3 is required to generate the scope sweep trigger. The net number of events after the target Full-Empty subtraction was zero. This indicates that they were not elastic scatters which were lost because of missing signals from one H_3 counter. Assuming that events of this type are the result of lost pulses from all H_3 counters, we found an average H_3 "pulse recording" efficiency of 98%. The frequency spectrum of (i, j) for these events was similar to that found for all measured events. We concluded therefore that the inefficiency implied by the existence of this type of event could only introduce an uncertainty in the results which was not a function of angle. Because of the large statistical uncertainties ($\approx$ 20%) that exist, the uncertainties introduced by this effect are insignificant.

Table IV. Hodoscope film-scanning results.

	Momentum (Bev/c)					
	0.97		1.17		1.97	
	Full	Empty	Full	Empty	Full	Empty
Total sweeps	6800	797	9316	1665	13 214	2841
Number analyzed	1871	320	2922	721	5424	1408
Elastic scatters	494	64	791	157	1544	263
N_K	1.035×10^6	0.176×10^6	1.503×10^6	0.404×10^6	2.437×10^6	0.788×10^6
h_5/N_K	0.312	0.371	0.385	----	0.566	0.624

d. H_1 missing (< 1%). No angular dependence different from that for the analyzed events was found. These events also disappear in the Full-Empty subtraction.

e. Any two of the hodoscope signals missing (<1%).

f. More than two particles through any of the hodoscope arrays(1%). These were beam accidentals, interactions in the aluminum of the target walls and spark chamber, or decays.

The origin of the K^+ proton scatters could not be determined precisely from the hodoscope information. However, the region of the Z axis through which the line of scatter passes provides some information on the distribution of origins. A plot of the expected Z-intercept distribution for a given angle of scatter is shown in Fig. 14; the experimental distribution found for the 1.97-Bev/c data is also shown for comparison. The theoretical curve was plotted by assuming a Gaussian beam distribution cut off at ±2 in. Similar plots of the data were made at all angles, where data was sufficient, to check that events accepted as hydrogen scatters were coming from the hydrogen target.

The calculated cross sections are presented in Table V. The data accumulated at 1.17 and 0.97 Bev/c were not sufficient to provide significant measurements in more than one or two angular intervals. The quoted errors are statistical.

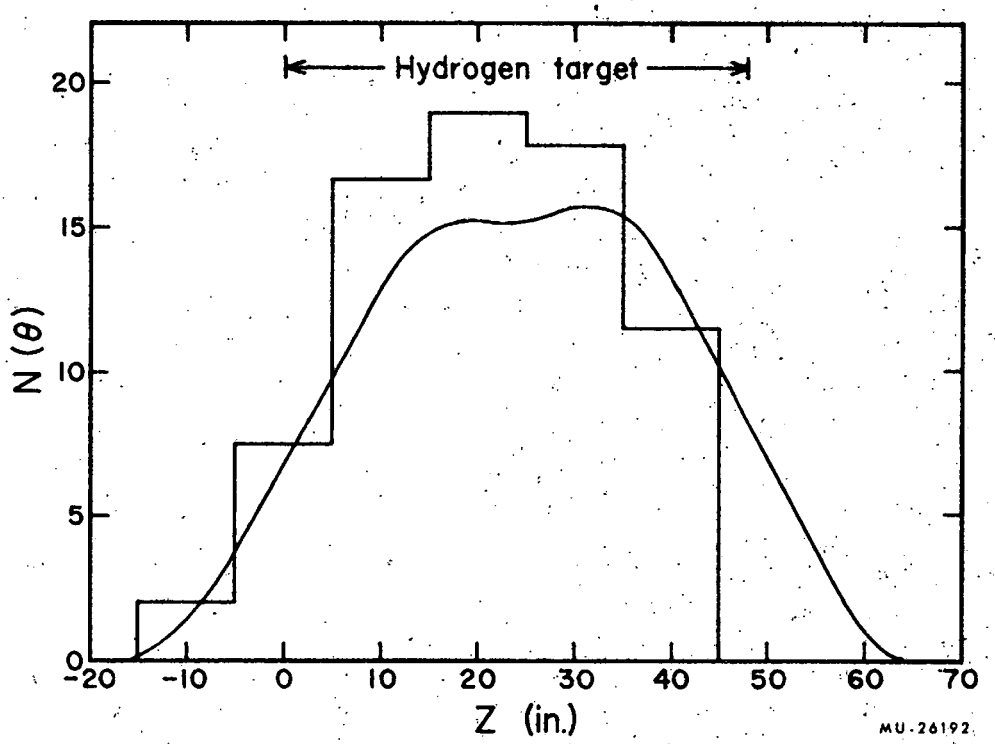

Fig. 14. The Z intercept of particles scattered through 6.8 deg. The solid curve was calculated for a Gaussian beam distribution symmetric about the Z axis.

Table V. Differential cross sections in the c.m. system, measured with the hodoscope apparatus.

1.97 Bev/c			1.17 Bev/c			0.97 Bev/c		
θ^*	N^a	$\frac{d\sigma}{d\Omega}$(mb/sr)	θ^*	N^a	$\frac{d\sigma}{d\Omega}$(mb/sr)	θ^*	N^a	$\frac{d\sigma}{d\Omega}$(mb/sr)
8.1	153±38	5.21±1.29	9±2	150±41	3.36±0.92	15±8	92±30	2.40±0.78
10.7	117±30	4.36±1.12	20±5	120±21	2.36±0.45			
13.3	119±23	3.94±0.80						
15.8	80±17	2.62±0.56						
18.3	81±14	2.62±0.45						
20.7	62±14	2.08±0.47						
23.1	57±14	1.94±0.48						
25.4	48±8	2.08±0.41						
27.7	39±7	2.41±0.43						
29.8	23±6	2.75±0.72						

[a]The net number of elastic scatters after the Full-Empty subtraction.

V. DISCUSSION

A. Phase-Shift Analysis

1. Nonrelativistic scattering amplitudes. The differential cross section for K^+-p elastic scattering can be separated into two parts: one involving a change in orbital angular momentum (spin-flip), and the other conserving orbital angular momentum (nonflip). (We assume K spin = 0 and proton spin = 1/2.) The cross section can be written

$$\frac{d\sigma}{d\Omega}(\theta) = |A|^2 + |B|^2 \sin^2\theta , \tag{18}$$

where A is the nonflip amplitude and B is the spin-flip amplitude.

The amplitudes A and B for nuclear scattering can be written

$$A(\theta) = \frac{\lambda}{2i} \sum_{\ell=0}^{\infty} (\ell+1)\left[\eta_\ell^+ \exp(2i\delta_\ell^+) - 1\right] + \ell\left[\eta_\ell^- \exp(2i\delta_\ell^- - 1)\right] P_\ell(\cos\theta),$$

$$B(\theta) = \frac{\lambda}{2i} \sum_{\ell=1}^{\infty} \left[\eta_\ell^+ \exp(2i\delta_\ell^+ - \eta_\ell^-) \exp(2i\delta_\ell^-)\right] \frac{dP}{d(\cos\theta)}(\cos\theta), \tag{19}$$

where

λ = particle wavelength in c.m. system,

$P_\ell(\cos\theta)$ = ℓth order Legendre polynomial.

The complex phase shifts have been written

$$\left.\begin{aligned} \rho_\ell^\pm &= \delta_\ell^\pm + i\alpha_\ell^\pm \\ \text{and} \quad \eta_\ell^\pm &\equiv \exp(-2\alpha_\ell^\pm) \end{aligned}\right\} \quad \text{for } j = \ell \pm 1/2 . \tag{20}$$

The amplitudes for pure Coulomb scattering can be written in the same form,[17] with the absorption parameters $\eta_\ell = 1$. When both nuclear and Coulomb forces are present the scattering amplitudes can again be written in the form (19), where the phase shifts are the result of the "total interaction" (nuclear plus Coulomb). In the following discussion $\delta_\ell^\pm$ will refer to the total interaction phase shifts.

In the partial-wave analysis it is desirable to terminate the summation (19) with as low an ℓ valve as is needed to fit the experimental data. The short-range nuclear potential affects only those partial waves up to about $\ell_{max} \approx \frac{R}{\lambda}$, where R is the range of the nuclear potential, and λ is the particle wavelength in the c.m. system. The infinite-range Coulomb potential, on the other hand, effects all orders of ℓ.

A partial-wave expansion that converges more rapidly than the form given in (19) has been given by Foote.[18] Briefly, the derivation proceeds as follows.

First we note that the nonrelativistic-Coulomb amplitudes (for spinless particles) can be written in the closed form[19]

$$A_c(\theta) = \frac{\lambda m}{2\sin^2(\theta/2)} \exp\left\{- i n \ln[\sin^2(\theta/2) + i\pi + 2 i \eta_0]\right\}, \tag{21}$$

where

$$\eta_0 = \arg \Gamma (1 + i n),$$

$$n = \frac{e^2}{\hbar c} (\beta_K)_{lab}$$

Now we can write the scattering amplitudes for the total interaction as

$$A_T(\theta) = A_C(\theta) + [A_T(\theta) - A_C(\theta)],$$

$$B_C(\theta) = 0 \text{ (nonrelativistic)}. \tag{22}$$

Using (19), (21), and (22), we find

$$A_T(\theta) = \frac{\lambda n}{2\sin^2(\theta/2)} \exp\left\{- i n \ln[\sin^2(\theta/2)] + i\pi + 2i\eta_0\right\}$$

$$+ \frac{\lambda}{2i} \sum_{\ell=0}^{\infty} \left\{(\ell+1)[\eta_\ell^+ \exp(2i\delta_\ell^+) - \exp(2i\phi_\ell)]\right.$$

$$\left. + \ell(\eta_\ell^- \exp(2i\delta_\ell^-) - \exp(2i\phi_\ell))\right\} P_\ell(\cos\theta), \tag{23 cont.}$$

$$B_T(\theta) = \frac{\lambda}{2i} \sum_{\ell=1}^{\infty} \eta_\ell^+ \left[\exp(2i\delta_\ell^+) - \exp(2i\phi_\ell) \right] \frac{d[P_\ell(\cos\theta)]}{d(\cos\theta)} , \tag{23}$$

where

$$\phi_\ell = \sum_{k=1}^{\ell} \tan^{-1}(n/k).$$

The ϕ_ℓ are the difference between the nonrelativistic Coulomb phase shifts of order ℓ and order $\ell = 0$. The nuclear phase shifts are approximately given by

$$\delta_\ell^{\pm}(\text{nuc.}) \approx \delta_\ell^{\pm} - \phi_\ell .$$

2. First-order relativistic corrections. Solmitz[20] has calculated the relativistic Coulomb scattering amplitudes for the scattering of spin-zero particles by spin-1/2 particles. The Coulomb nonflip and spin-flip amplitudes for K^+ on protons are

$$A_c(\text{rel.}) = -\frac{\lambda e^2}{2\hbar c} \frac{\left[1 + \frac{\beta_k\beta_p}{2}(1+\cos\theta) - (2\mu_p - 1)(1-\cos\theta)\frac{\beta_p^2}{4}\right]}{(\beta_k + \beta_p)\sin^2(\theta/2)}$$

$$= -\frac{n}{2\sin^2(\theta/2)} + \frac{\lambda n\, \beta_k\beta_p + (2\mu_p - 1)\frac{\beta_p^2}{2}}{1 + \beta_k\beta_p} , \tag{24}$$

$$B_c(\text{rel.}) = \frac{\lambda^2 e^2}{2\hbar c} \frac{\left[\frac{\mu_p\beta_k\beta_p}{2} + (2\mu_p - 1)\frac{\beta_p^2}{4}\right]\sin\theta}{(\beta_k + \beta_p)\sin^2(\theta/2)}$$

$$= \frac{\lambda n}{2\sin^2(\theta/2)} \left[\frac{\mu_p\beta_k\beta_p}{2} + 2(\mu_p - 1)\frac{\beta_p^2}{4}\right] \sin\theta , \tag{25}$$

where β_k and β_p are the c.m. velocities of the K and proton, μ_p is the proton magnetic moment in nuclear magnetons, and n is as defined in Eq. (21).

Corrections to the nonrelativistic total phase shifts and to the spin-flip amplitude can be calculated from the second term of (24) and from (25). Note that the first term in (24) differs only in phase from the nonrelativistic Coulomb amplitude. Such a calculation has been carried out by Foote,[18] in which the correction terms are expanded in partial waves and applied to the nonrelativistic amplitudes term by term. The final amplitudes are

$$A_T(\theta) = -\frac{\lambda n}{2\sin^2(\theta/2)} \exp\left\{-i n \ln\left[\sin^2(\theta/2)\right]\right\}$$

$$+ \frac{\lambda}{2i} \sum_{\ell=0}^{\ell_{max}} \left\{(\ell+1)\left[\eta_\ell^+ \exp(2i\delta_\ell^+) - \exp(2i\phi_\ell)\right] + \ell\left[\eta_\ell^- \exp(2i\delta_\ell^-) - \exp(2i\phi_\ell)\right]\right\} P_\ell(\cos\theta), \tag{26}$$

$$B_T(\theta) = \frac{\lambda n C \sin\theta}{2\sin^2(\theta/2)} + \frac{\lambda}{2i} \sum_{\ell=1}^{\ell_{max}} \left\{\eta_\ell^+ \exp(2i\delta_\ell^+) - \eta_\ell^- \exp(2i\delta_\ell^-) - n C\left[\frac{2\ell+1}{\ell(\ell+1)}\right]\right\} \times \frac{d[P(\cos\theta)]}{d(\cos\theta)} . \tag{27}$$

where $$C = \frac{\left(\frac{\mu_p \beta_k \beta_p}{2}\right) + \left[(2\mu_p - 1)\left(\beta_p^2/4\right)\right]}{1 + \beta_k \beta_p} ,$$

and the nuclear phase shifts are approximately

$$\delta_\ell^\pm (\text{nuc.}) \approx \delta_\ell^\pm - \phi_\ell - \Delta\phi_\ell^\pm . \tag{28}$$

The first order relativistic corrections to the Coulomb phase shifts are

$$\Delta\phi_0 \approx n\left[\frac{\beta_k\beta_p + (2\mu_p - 1)\,\beta_p^2/2}{1 + \beta_k\beta_p}\right],$$

$$\Delta\phi_\ell^+ \approx \frac{n\,C}{\ell+1} \quad \text{for} \quad \ell \geq 1\,,$$

$$\Delta\phi_\ell^- \approx \frac{n\,C}{\ell} \quad \text{for} \quad \ell \geq 1\,. \tag{29}$$

3. Phase-shift-fitting procedure. A least-squares-fitting computer program[21] was used to find sets of phase shifts $(\eta_\ell^\pm,\ \delta_\ell^\pm)$ which resulted in a good fit of the differential cross section calculated from (26) and (27) to the experimental data. The usual χ^2 distribution analysis was used to determine goodness of fit, with

$$\chi^2 = \sum_i \left\{ \left| \frac{Y_i - (1+\epsilon)y_i}{\Delta y_i} \right|^2 + \left| \frac{\sigma_T - \sigma(\eta,\delta)}{\Delta\sigma_T} \right|^2 + \left| \frac{\epsilon}{\Delta\epsilon} \right|^2 \right\}, \tag{30}$$

where

$$Y_i = |\,A_T(\theta_i)\,|^2 + |\,B_T(\theta_i)\,|^2\,,$$

$$y_i = \frac{d\sigma}{d\Omega}(\theta_i)\ \text{(experimental)}\,,$$

ϵ = normalization parameter,

$\Delta\epsilon$ = uncertainty in normalization of experimental differential cross sections,

σ_T = experimental value for total cross section,

$\Delta\sigma_T$ = uncertainty in σ_T,

$\sigma(\eta, \delta)$ = total cross section calculated from the phase shifts.

The search proceeded from an initial set of phase shifts that were randomly selected on the intervals $-90 \text{ deg} < \delta < 90 \text{ deg}$ and $0 < \eta \leq 1.0$. About 100 trials were made at each momentum.

4. Results of the phase-shift analyses. Searches for S- and P-wave fits at both momenta produced several different sets of "good" phase shifts. In addition to the usual ambiguities there are various combinations of η's and δ's which gave good fits. Some of the solutions which were found with $P(\chi^2) \gtrsim 0.05$ are presented in Table VI.

Phase-shift analyses at lower momenta[10,22] have yielded (most probable) solutions with large S-wave phase shifts. Rapid variations in the S-wave phase shift as a function of energy are unlikely. Thus the "reasonable" phase shift sets in Table VI are probably those with $\delta_0 \approx 30$ deg to 50 deg. This cannot be made very precise, of course, but with the information available at the present time it appears to be the only criterion which can be used to narrow down the range of possible solutions.

The data at small angles are not good enough to determine the sign of the nuclear interaction. However, the solutions which require constructive interference between the nuclear and Coulomb interactions give consistently slightly better fits than those requiring destructive interference. Since this is in agreement with the results at lower energies we are encouraged to accept solutions which produce negative values for the real part of the forward scattering amplitude (D).

We observe that all solutions for the 0.97-Bev/c data give values for the magnitude of D which are equal, within statistics. The values of D that were used in the dispersion relation analysis were those calculated for the A^- solutions given in Table VI.

The measured angular distributions and representative phase-shift solutions are plotted in Fig. 15.

Table VI. Phase-shift solutions found at 0.97 Bev/c and 1.17 Bev/c.

	δ_0	η_0	δ_1^-	η_1^-	δ_1^+	η_1^+	D(f)	$P(\chi^2)$
0.97 Bev/c								
A^-	-38±1	1.0	-10±1	1.0	3±4	0.6	-0.10±0.03	0.14
A^+	39±1	1.0	-16±1	0.9	1±3	0.7	+0.09±0.03	0.07
B^-	30±1	0.4	-38±2	0.8	-4±2	1.0	-0.12±0.04	0.15
B^+	-32±1	0.5	39±3	0.7	5±2	1.0	+0.12±0.04	0.07
C^-	9±1	0.7	15±7	1.0	-29±2	0.8	-0.12±0.04	0.13
C^+	-14±1	0.7	-14±7	1.0	29±2	0.8	+0.10±0.03	0.06
D^-	3±1	0.8	-43±3	0.9	7±9	0.8	-0.10±0.03	0.11
E^-	-20±9	1.0	39±9	0.7	-10±1	0.8	-0.10±0.03	0.12
1.17 Bev/c								
A^-	-33±2	1.0	-10±19	0.8	4±1	0.2	-0.19±0.09	0.22
A^+	43±2	0.8	5±1	0.6	-9±5	0.4	+0.08±0.08	0.07
B^-	74±1	0.2	-30±9	0.6	-14±3	0.8	-0.19±0.09	0.21
C^-	- 3±1	0.2	-64±14	0.3	-15±1	0.9	-0.20±0.09	0.22
C^+	12±5	0.2	55±10	0.6	11±2	0.8	+0.22±0.10	0.08
D^-	- 9±1	0.3	1±5	1.0	-39±1	0.5	-0.18±0.10	0.21
D^+	13±1	0.4	- 1±9	1.0	43±2	0.4	0.17±0.10	0.10

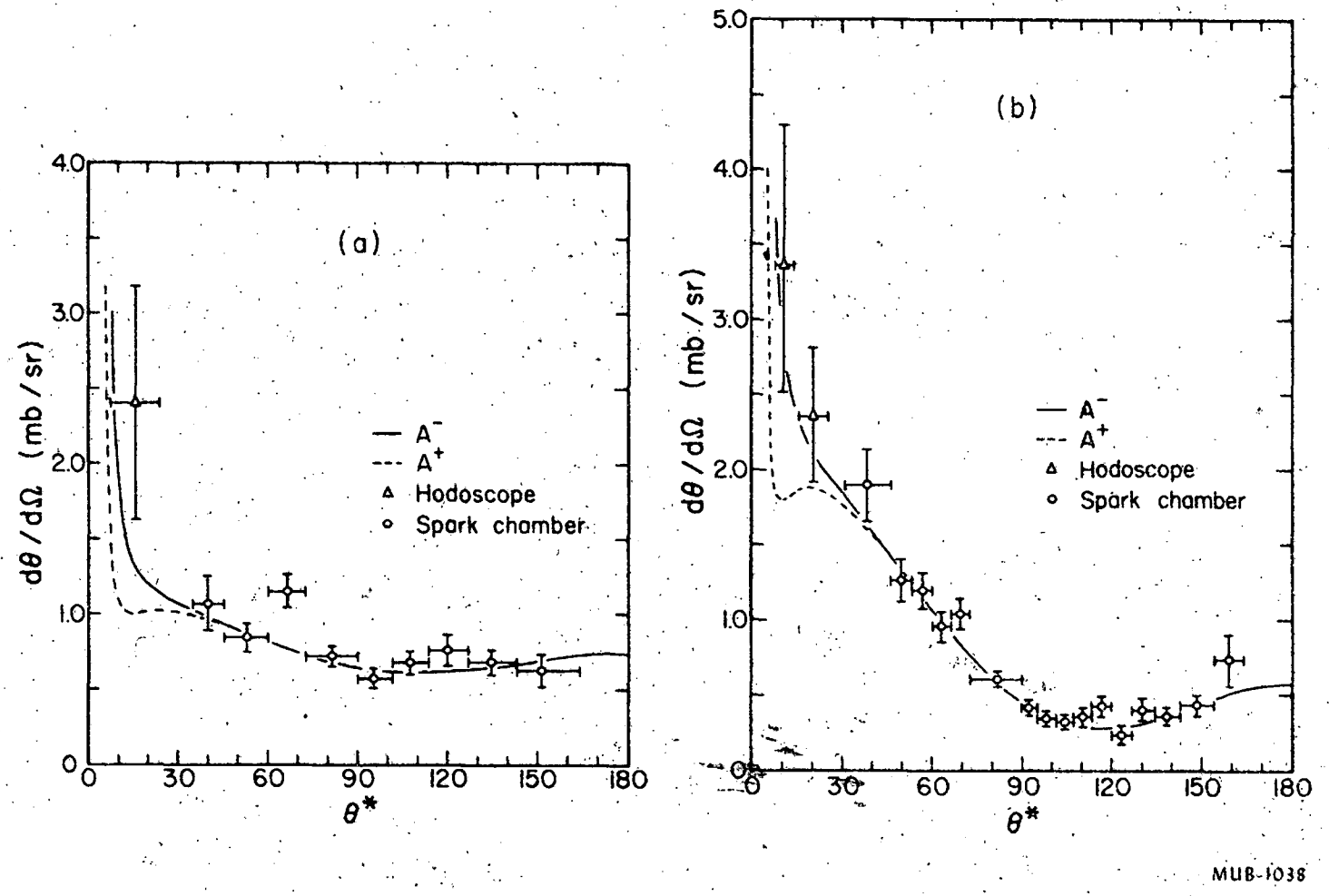

Fig. 15. Angular distributions and representative phase shift solutions for (a) 0.97 Bev/c and (b) 1.17 Bev/c.

B. Small-Angle Scattering at 1.97 Bev/c

The elastic-scattering cross section at 1.97 Bev/c is peaked in the forward direction. This implies that many angular momentum states are present. For this reason a partial wave analysis was felt to be impractical with the small angle data available from this experiment. Since there are many angular momentum channels open at this momentum, and because the measured angular distribution is dominated by the diffraction peak, an optical model fit to the data was attempted.

A model was used in which the transmission rate for a given impact radius ρ is given by

$$1 - a = C\, g(\rho), \tag{31}$$

where C is complex if there is real scattering.[8] A good fit was obtained with a Gaussian shape,

$$g(\rho) = \exp\left(-\rho^2 / \left\langle \rho^2 \right\rangle\right) \tag{32}$$

where $\sqrt{\langle \rho^2 \rangle}$ is the rms radius of the disc.

The differential cross section is given by

$$\frac{d\sigma}{d\Omega} = \sigma_0 \exp\left(-q^2 \left\langle \rho^2 \right\rangle / 2\right) \tag{33}$$

where $q = 2p \sin(\theta/2)$ is the momentum transfer.

The parameters to be determined from the data are σ_0 = forward elastic scattering cross section, and $\sqrt{3/2}\left\langle \rho^2 \right\rangle^{1/2}$ = interaction radius.

A least-squares fitting procedure was used to determine the best values for σ_0 and $\left\langle \rho^2 \right\rangle^{1/2}$. The results of this analysis are presented in Table VII, and a plot of the cross section calculated from (33) and the experimental data are presented in Fig. 16.

Table VII. Best values found for the parameters discussed in the text. D is the real part of the forward scattering amplitude in units where $M_K = \hbar = c = 1$.

Case	$\sqrt{3/2 < \rho^2 >}$ (f)	σ_0(mb)	$D(\lambda_K)$	$P(\chi^2)$
1. All points	0.65±0.06	4.0±0.5	0.22±0.14	0.25
2. Excluding two points at largest angles	0.92±0.11	4.9±0.8	1.0 ±0.4	0.60

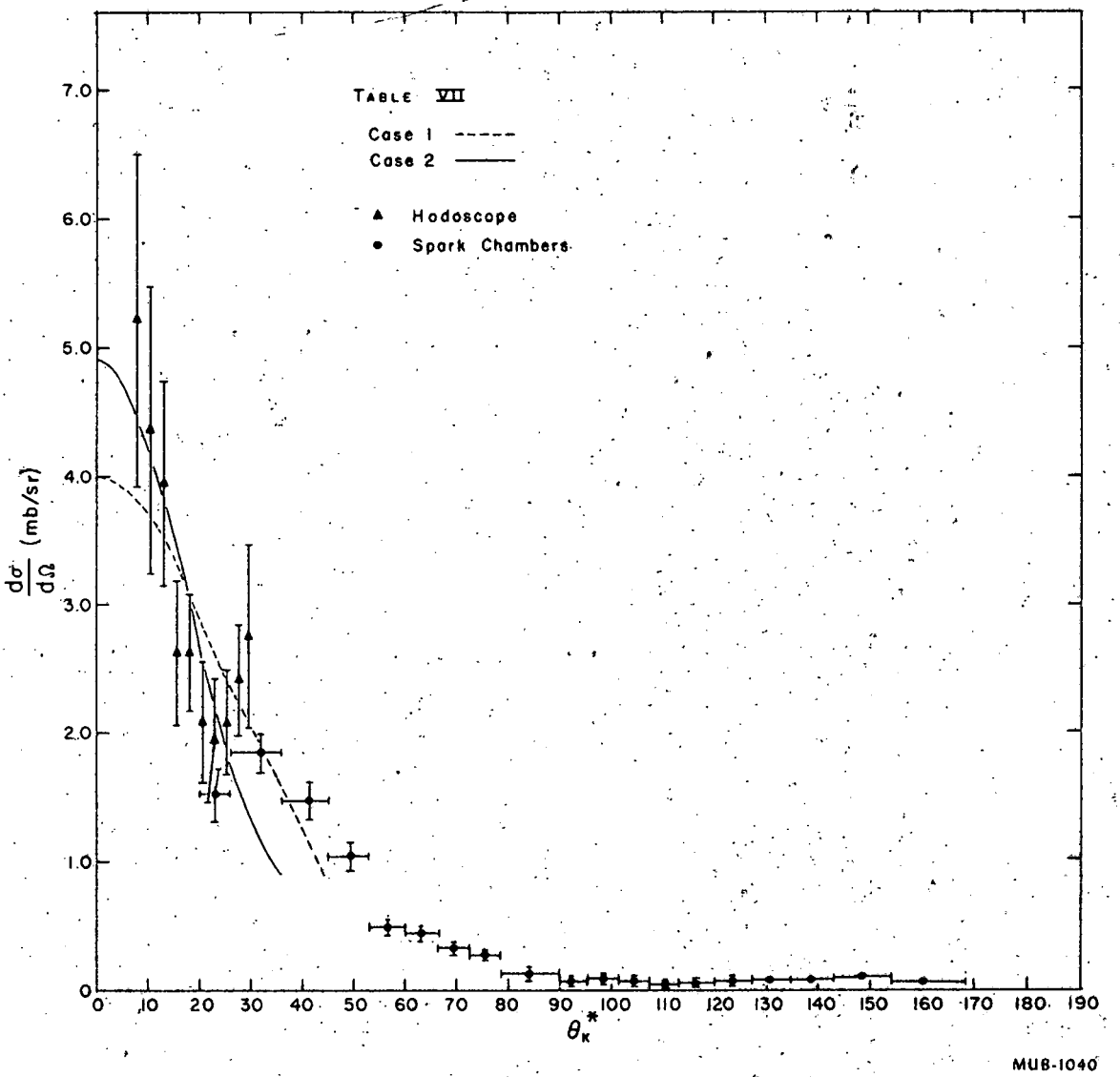

Fig. 16. Elastic scattering at 1.97 Bev/c. The curves were calculated using Eq. (33).

The solution for Case 1 gives a better fit to the small-angle spark-chamber data than the solution for Case 2. It is to be noted that the interaction radius found for Case 1 is smaller than that found for K^--p scattering at the same energy,[8] namely

$$\sqrt{3/2\langle\rho^2\rangle} = 0.96\pm0.04 \text{ f.}$$

The solution for Case 2 gives a value for the K^+-p interaction radius that is about the same as that found for K^--p.

C. Dispersion Relations

The formalism for constructing dispersion relations for two-particle systems has been discussed by many authors in recent years. A particularly lucid account has been given by Chew.[3] A derivation of K-N forward dispersion relations based on the methods described in this paper is given in Appendix B. Many authors have written down K-N dispersion relations in analogy with π-N relations. A derivation which proceeds from the Mandelstam representation for the invariant scattering amplitude is included in this report for completeness.

The forward dispersion relations relate the real part of the forward scattering amplitude to integrals over the imaginary parts for scattering in the cross channels as well as the incident channel. In units where $h = c = M_K = 1$ we find

$$D_{\pm}(\omega) = C + \frac{\tilde{\Gamma}}{\tilde{\omega} \pm \omega} + \frac{1}{\pi}\int_{\omega_{\Lambda\pi}}^{\infty} \frac{A_-(\omega')d\omega'}{\omega' \pm \omega} + \frac{1}{\pi}\int_1^{\infty} \frac{A_-(\omega')d\omega'}{\omega' \pm \omega}$$

$$+ \frac{1}{\pi}\int_1^{\infty} \frac{A_+(\omega')d\omega'}{\omega' \mp \omega} \quad . \tag{34}$$

The pole term $\frac{\tilde{\Gamma}}{\tilde{\omega}+\omega}$ is an average pole combining the effects of the Λ, Σ, Y_1^*, and Y_0^* poles (see Appendix B). $D_{\pm}(\omega)$ is the real part and $A_{\pm}(\omega)$ is the imaginary part of the $K^{\pm}$-p forward scattering amplitude.

Fig. 17. The imaginary part of the forward scattering amplitude for K^+-p and K^--p elastic scattering. The optical theorem was used to calculate the experimental points from the measured total cross sections.

Symbol code: The numbers beside the symbols are for determining references from the following sequence: (1) Ref. 13; (2) Ref. 22; (3) Burrowes et al., Ref. 11; (4) Vovenko et al., Ref. 11; (5) E. W. Jenkins, W. F. Baker, R. L. Cool, T. F. Kycia, R. H. Phillips, A. L. Read, Bull. Am. Phys. Soc. 6, 433 (1961); (6) Ref. 9; (7) Ref. 10; (8) O. Chamberlain, K. M. Crowe, D. Keefe, L. T. Kerth, A. Lemonick, Tin Maung, T. F. Zipf, Phys. Rev. 125, 1696 (1962); (9) Ref. 8; (10) M. Ferro-Luzzi, R. D. Tripp, M. B. Watson, Phys. Rev. Letters 8, 28 (1962); (11) von Dardel et al., Ref. 11; (12) same as (5).

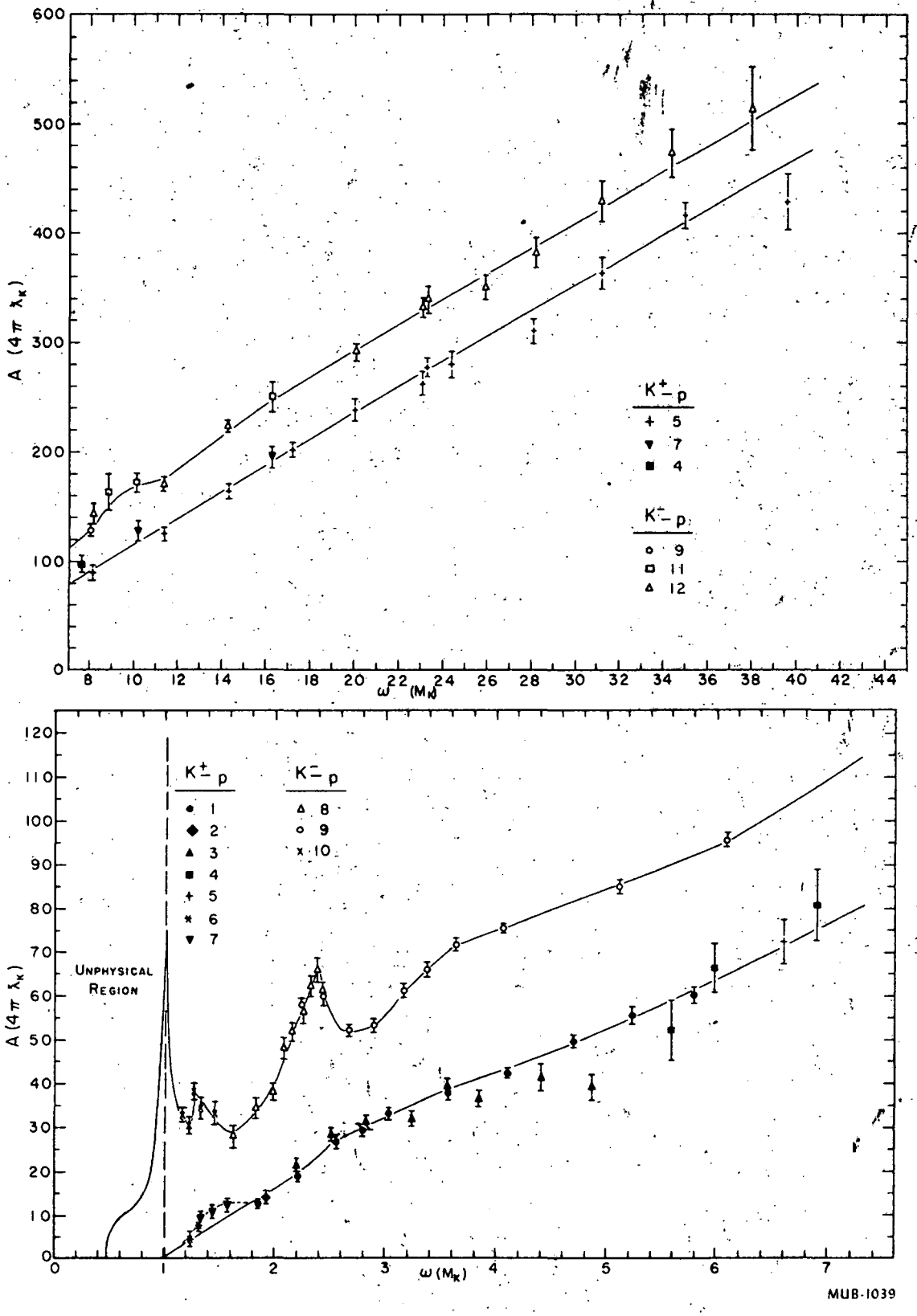
A (4π λ̄K²)
ω (MK)
K+ p
+ 5
▼ 7
■ 4
K− p
○ 9
□ 11
△ 12
K+ p
● 1
◆ 2
▲ 3
■ 4
+ 5
* 6
▼ 7
K− p
△ 8
○ 9
x 10
UNPHYSICAL REGION
MUB-1039

and $\omega = \sqrt{p^2+1}$ is the total laboratory energy of the K. The quantity C is independent of the energy ω.

The objects of the present analysis are to evaluate the average pole residue $\tilde{\Gamma}$ and to compare the predicted energy dependence of D with the experimental data. This can be achieved if the other terms in (34) can be evaluated. The imaginary part of the forward scattering amplitude, in the physical energy region ($\omega \geq 1$), is related to the total cross section by the optical theorem

$$\text{Im } f\,(\theta = 0) \equiv A(\omega) = \frac{\sqrt{\omega^2-1}\,\sigma(\omega)}{4\pi} .$$

Values for $A_{\pm}(\omega)$ calculated from all the measured total cross sections extant to this date are plotted against ω in Fig. 17. The integrals over the physical region (up to $\omega = 40$) were evaluated numerically for several possible curves drawn through the experimental data. The integrals in (34) do not converge. To ensure convergence and to eliminate the constant in (34), subtracted relations must be formed.

The treatment of the region beyond which experimental data are available ($\omega > 40$), and the unphysical continuum, are discussed in Appendix B.

The other quantities in (34) which are directly measurable are the real parts of the forward scattering amplitudes $D_{\omega}(\omega)$. The values that are available, including the best values measured in this experiment, are given in Table VIII.

1. Subtractions. At least one subtraction must be made to eliminate the constant term in the expression for $D_+(\omega)$ or $D_-(\omega)$. The purpose of forming more complicated subtracted relations is to ensure more rapid convergence of the integrals and to reduce the importance of some energy regions in evaluating the integrals in (34).

The following are typical of single subtractions which have been used.

$$D_+(\omega_1) - D_+(\omega_2) = \frac{\tilde{\Gamma}(\omega_2-\omega_1)}{(\tilde{\omega}+\omega_1)(\tilde{\omega}+\omega_2)} + \frac{\omega_2-\omega_1}{\pi}\int_{\omega_{A\pi}}^{1} \frac{A_-(\omega')d\omega'}{(\omega'+\omega_1)(\omega'+\omega_2)}$$

$$+ \frac{(\omega_2-\omega_1)}{\pi}\int_1^{\infty}\left[\frac{A_-(\omega')}{(\omega'+\omega_1)(\omega'+\omega_2)} - \frac{A_+(\omega')}{(\omega'-\omega_1)(\omega'-\omega_2)}\right] d\omega' , \quad (35)$$

$$D_+(\omega) - D_-(\omega) = \frac{2\omega\,\tilde{\Gamma}}{(\omega^2 - \tilde{\omega}^2)} + \frac{2\omega}{\pi}\int_{\omega_{A\pi}}^{1} \frac{A_-(\omega')d\omega'}{\omega'^2 - \omega^2}$$

$$+ \frac{2\omega}{\pi}\int_1^{\infty} \frac{(A_-(\omega') - A_+(\omega'))}{\omega'^2 - \omega^2}\, d\omega' . \quad (36)$$

The convergence of the last integral in these expressions has been discussed by Amati et al.[23] They find that if the condition, $\lim_{\omega\to\infty} \frac{A_\pm(\omega)}{\omega}$ = constant, is valid, then the integrals of the form

$$\int_{\omega_0}^{\infty} \frac{A_-(\omega') - A_+(\omega')}{\omega'^2}\, d\omega' \quad \text{converge.}^{24}$$

Udgaonkar[25] has considered the asymptotic behavior of the quantities $(\sigma_- + \sigma_+)$ and $(\sigma_- - \sigma_+)$ assuming that Regge poles dominate the cross sections at high energies. His results provide a means of evaluating the integrals above the cutoff energy $\omega = 40$. (See Appendix B.)

Table VIII. Experimental values of the real part of the forward scattering amplitude in the laboratory system, in K-Compton wavelengths ($\hbar = c = M_K = 1$).

ω	D	Reference
1.23	-1.14±0.05	26[a]
1.28	-1.23±0.14	10[a]
1.46	-1.14±0.05	26[a]
1.46	-1.20±0.08	10[a]
1.85	-1.02±0.05	26[a]
1.92	-0.80±0.23	Solution A^- of reference 22[b]
2.22	-0.46±0.19	Table VI, Solution A^-
2.56	-0.94±0.44	Table VI, Solution A^-
4.10	±2.2 ±0.9	Table VIII, Case 2
-1.04	+0.6±1.7	30
-1.08	-0.3±1.1	30
-4.10	±3.3±0.6	8

[a]These values were calculated from the measured total cross sections by using

$$D(\omega) = \frac{k_L}{k_{c.m.}} \sqrt{\frac{\sigma_T}{4\pi} - k_{c.m.}^2 \left(\frac{\sigma}{4\pi}\right)^2} .$$

[b]Calculated using $D(\omega) = \frac{\lambda}{2} \Sigma [(\ell+1)(\eta_\ell^+ \sin 2\delta_\ell^+) + \ell \eta_\ell^- \sin 2\delta_\ell^-]$.

2. Results. An attempt was made to take fullest advantage of the available data by plotting

$$f(\omega,\tilde{\Gamma}) = \frac{\tilde{\Gamma}(1-\omega)}{(\tilde{\omega}+\omega)(\tilde{\omega}+1)} = D(\omega)-D(1)+I(1)-I(\omega), \tag{37}$$

where

$$I(\omega) = \frac{(1-\omega)}{\pi}\int_{\omega_{\Delta\pi}}^{1} \frac{A_-(\omega')d\omega'}{(\omega'+\omega)(\omega'+1)} + \frac{(1-\omega)}{\pi}\int_{1}^{\infty}\left[\frac{A_-(\omega')}{(\omega'+\omega)(\omega'+1)} - \frac{A_+(\omega')}{(\omega'-\omega)(\omega'-1)}\right]d\omega'$$

The right-hand side of (37) is known at several energies where the real part of the forward scattering amplitude has been measured. The function $f(\omega,\tilde{\Gamma})$ was plotted for various values of $\tilde{\Gamma}$, and the $\tilde{\Gamma}$ which gave the best fit to the experimental data was found. A careful statistical fit cannot be made until more K^--p elastic scattering data are obtained. The value $\tilde{\Gamma} = -1.0\pm1.0$ gives a good fit to the K^+-p data but does not fit the experimental values for the K^--p data. (See Fig. 18). These numbers are preliminary and do not represent the best values one can get from the data presently available.

A more complete study of the results one can get from the application of forward dispersion relations to the K-N data is underway. A subtracted form which removes the Y_1^* pole from the residue term has been used by G. Goldhaber and his collaborators.[26] Preliminary results indicate that the remaining residue (Λ, Σ, and, possibly, Y_0^* poles) is positive, opposite in sign to our value for the total effective pole. It is possible that the Y_1^* residue is large and negative, thus accounting for this difference in sign. Uncertainties in the experimental data make an unambiguous solution unlikely at the present time.

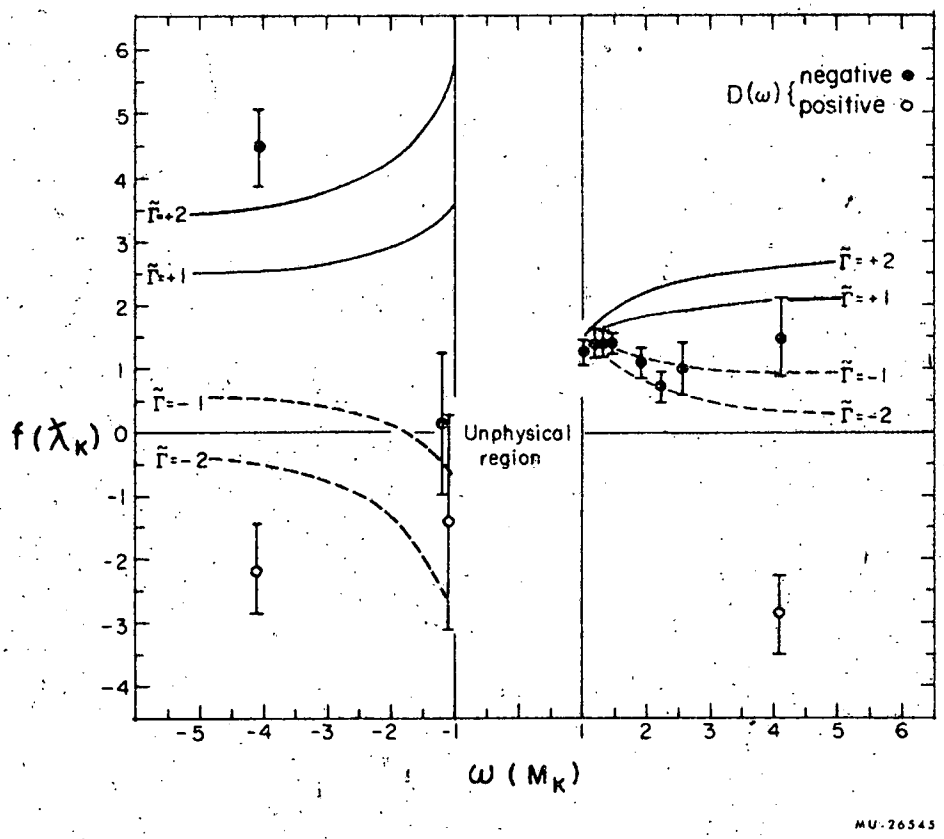

Fig. 18. The function $f(\omega, \tilde{\Gamma})$ plotted for $\tilde{\Gamma} = -1$ and $\tilde{\Gamma} = -2$. values for $D(\omega)-D(1)+I(1)-I(\omega)$ are plotted at all ω for which $D(\omega)$ has been measured.

VI. CONCLUSIONS

The energy dependence of the K^+-p total cross section appears to be S-wave up to about 0.8-Bev/c momentum. In the region of the 2π production threshold there is a shoulder in the total cross section and a slowly decreasing elastic cross section. This behavior is illustrated in Fig. 19 by the curves that are drawn through the experimental points. (The curves have no other significance.) It is seen that the total cross section cannot be pure S-wave beyond about 0.8 Bev/c.

The phase-shift analysis at 0.97 and 1.17 Bev/c indicated an increasing P-wave contribution to the elastic scattering, as expected from the discussion above. We were unable to obtain a unique set of phase shifts; however, all solutions indicated the presence of considerable P-wave interaction.

We were able to determine values for the real part of the forward elastic-scattering amplitude at 0.97, 1.17 and 1.97 Bev/c. These quantities were used in a forward dispersion relation calculation. The results are, as is usual with these calculations, rather imprecise. They do indicate areas where more data would be useful. We are encouraged by the rather good fit to the measured values for $D_+(\omega)$; that is, for K^+-p scattering. For the average pole residue we found $\Gamma \approx -1.0$. This is the residue of an effective pole including the Λ, Σ, and Y_1^* poles, and possibly the Y_0^* pole.

The existence of the Y_1^* and Y_0^* poles complicate the problem of determining the ΛKN and ΣKN relative parities. These complications are discussed by Dalitz.[27] At present we can say only that our negative value for the composite pole residue is consistent with even $\Lambda\Sigma$ relative parity, which is the result found by Tripp et al.[28]

We wish to emphasize that our analysis cannot separate the effects of the various pole terms on K^+-p scattering, thus making a determination of the $K\Lambda N$ parity practically impossible. However, it is of interest to attempt to fit the real part of the scattering amplitude as a function of energy to the predictions of dispersion theory.

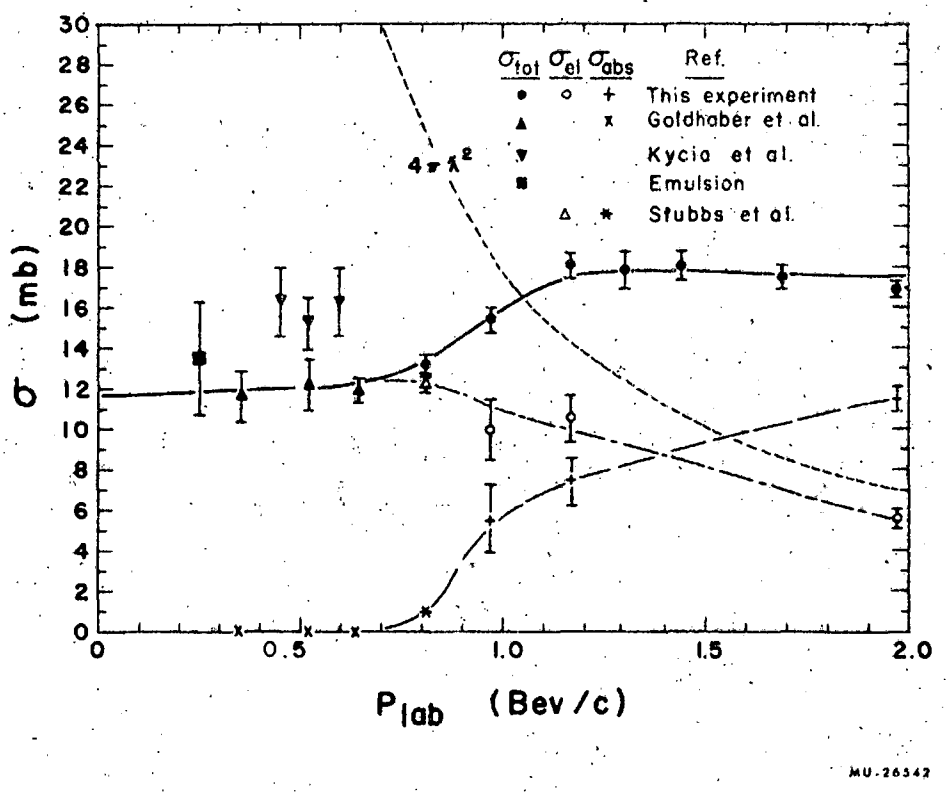

Fig. 19. The K^+-p total, elastic, and inelastic cross sections in the momentum range p_{lab} = 0 to 2 Bev/c. The curves through the measured cross sections have no theoretical significance.

ACKNOWLEDGMENTS

It is a pleasure to acknowledge the guidance and encouragement of Professor L. T. Kerth throughout the author's graduate career. The advice and assistance of Dr. D. Keefe, Dr. P. G. Murphy, Dr. W. A. Wenzel, and Dr. T. Zipf have been extremely valuable. The author is particularly indebted to Mr. W. Holley for his assistance with the data analysis and for many enlightening discussions. The assistance of Mr. C. Noble during the execution of the experiments is gratefully acknowledged.

Thanks are due Mr. John Shively for his work in designing and testing the spark-chamber vacuum boxes. The author thanks Mr. C. Burton, Mr. R. Duncan, Mr. D. Linn, and Mr. G. Schnurmacker for their valuable assistance in setting up and running the experiment. The efforts of Mr. D. Barefoot, Mr. W. Blake, Mr. C. Burton, Mr. R. Duncan, and Mr. J. Greenwood who scanned the film are greatly appreciated.

The cooperation of the Bevatron operating crew under Dr. E. Lofgren during the experimental run was appreciated.

This work was done under the auspices of the U. S. Atomic Energy Commission.

APPENDICES

A. Multiple-Scattering Correction to the Total Cross Sections

Consider a beam of K's traveling parallel to the central beam axis. We assume a radially symmetric beam in which the particle density at the transmission counter, assuming no multiple scattering in the hydrogen, is f(r). The total number of particles in the annulus dr at r is

$$n(r)dr = 2\pi r\, f(r)dr .$$

For this calculation we consider the hydrogen to be concentrated at the center of the target, thus neglecting the lateral diffusion of the beam in the target and the correlation between lateral displacement and scattering angle.

The rms projected scattering angle is given by

$$\langle\theta\rangle = \frac{15}{p\beta}\sqrt{\frac{L}{X_0}},$$

where

p = particle momentum,

β = particle velocity,

L = path length in scatterer,

X_0 = radiation length in the scattering medium.

The distribution of scattering angles is normal with mean $\theta = 0$ and standard deviation $\langle\theta\rangle$:

$$P(\theta) = \frac{1}{\langle\theta\rangle\sqrt{2\pi}}\exp(-\theta^2/2\,\langle\theta\rangle^2).$$

Particles which were at radius r in the unscattered beam will be distributed normally about r as a result of multiple scattering in the hydrogen. Writing the standard deviation in radial displacement from r as $\epsilon = \langle\theta\rangle d$, where d is the distance from the center of the hydrogen target to the T counter,

we have

$$dN(R) = \frac{n(r)}{\epsilon\sqrt{2\pi}} \exp\left[-(R-r)^2/2\epsilon^2\right] dr.$$

The total beam distribution is the result of a parallel beam undergoing multiple scattering in the hydrogen target, and is given by

$$N(R) = \int_0^\infty \frac{n(r)}{\epsilon\sqrt{2\pi}} \exp\left[-(R-r)^2/2\epsilon^2\right] dr .$$

Now $n(r)$ is a slowly varying function compared with $\exp\left[-(R-r)^2/2\epsilon^2\right]$. Then we can expand $n(r)$ in a Taylor series:

$$n(r) = n(R) + (R-r)\frac{dn}{dR} + \frac{1}{2}(R-r)^2 \frac{d^2n}{dR^2} ,$$

neglecting terms of higher order in $(R-r)$. Then we find

$$N(R) = n(R) + \frac{\epsilon^2}{2} \frac{d^2n}{dR^2} .$$

The number of particles that pass through a circular transmission counter is then

$$N_M = \int_0^{R_T} \left[n(R) + \frac{\epsilon^2}{2} \frac{d^2n}{dR^2}\right] dR$$

$$= N_T + \frac{\epsilon^2}{2} \left.\frac{dn}{dR}\right|_{R_T} .$$

where

N_T = number of particles which would pass through the T counter in the absence of multiple scattering, and

R_T = radius of T counter.

The correction to the transmission rate with target full is then

$$\Delta T_F = \frac{\Delta N_F}{N_0} = \frac{N_T - N_M}{N_0} \quad , \quad (N_0 = \text{number of } K^- \text{'s incident on the hydrogen target}),$$

and the correction to the total cross section is

$$\Delta\sigma = -\frac{1}{\rho_v L}\,\frac{\Delta T_F}{T_F} = -\frac{1}{\rho_v L}\left[\frac{\epsilon^2}{2N_M}\,\frac{dn}{dR}\Big|_{R_T}\right],$$

where

ρ_v = number of protons per unit volume,

L = length of hydrogen target,

N_M = number of particles that pass through the T counter with target full.

B. Derivation of Forward Dispersion Relations for K^--Proton Scattering

The derivation presented here follows the discussion given by Chew.[3] We include only enough preliminary remarks to define the problem and refer to reference 20 for theoretical justification.

1. Kinematics. Consider the diagram in Fig. B1. The four momenta $p_1, \cdots, p_4$, representing four ingoing particles, satisfy the conditions

$$\sum_{i=1}^{4} p_i = 0 \qquad \text{and} \qquad p_i^2 = M_i^2 \,. \tag{B-1}$$

It is convenient to use the invariants, $s_i = (p_i + p_4)^2$ (for $i = 1, 2, 3$), as variables in describing the scattering processes for the three channels listed below. Only two of the s variables are independent since they satisfy $\sum_{i=1}^{3} s_i^2 = \sum_{i=1}^{4} M_i^2$, where M_i = mass of the ith particle.

The assertion is now made that the invariant scattering amplitude $A(s_1, s_2, s_3)$ depends only on any two independent s variables, and not

on which of the p_i represent ingoing and which represent outgoing particles. The diagram in Fig. B1 represents the three processes

I. $K^- + p \rightarrow K^- + p$

II. $p + p^- \rightarrow K^+ + K^-$

III. $K^+ + p \rightarrow K^+ + p$.

2. Mandelstam representation. A prescription for the analytic continuation of the invariant scattering amplitude, which is symmetric in the s variables, has been given by Mandelstam. (Reference 3 includes this paper.) According to this prescription

$$A(s_1, s_2, s_3) = \sum_{i=1}^{3} \frac{1}{\pi} \int^{\infty} \frac{ds_i' \rho_i(s_i')}{s_i' - s_i} + \underbrace{\sum_{i=1}^{2} \sum_{j=2}^{3}}_{i \neq j} \frac{1}{\pi^2} \iint^{\infty} \frac{ds_i' ds_j' \rho_{ij}(s_i' s_j')}{(s_i' - s_i)(s_j' - s_j)} , \qquad \text{(B-2)}$$

where integration s extended from a lower limit greater than or equal to zero over the positive real axis. The spectral functions ρ_i and ρ_{ij} are real and satisfy the conditions

$$\rho_i(s_i) \neq 0 \quad \text{only when } s_i = M^2 ,$$

$$\rho_{ij}(s_i, s_j) \neq 0 \text{ only when } s_i \text{ or } s_j = M^2 ,$$

where M is the mass of a physical system having the same quantum numbers as the channel for which the corresponding s variable is the total energy in the c.m. system. The regions in which the spectral functions are nonvanishing are illustrated in Fig. B2. The lines along which the single spectral functions do not vanish lead to poles in the scattering amplitude (B-2). The poles which occur in the amplitude representing the reactions of Fig. B1 are

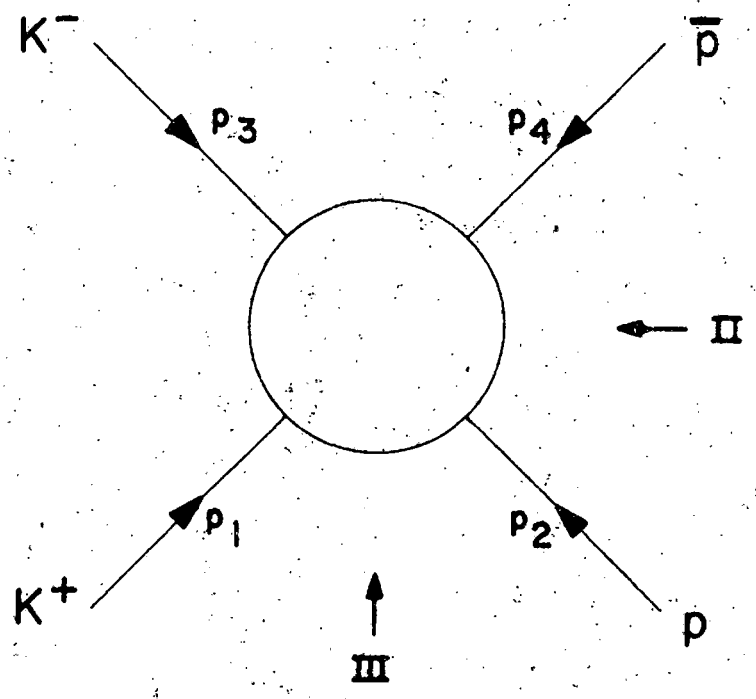

Fig. B1. Diagram defining the variables used in the dispersion-relation derivation.

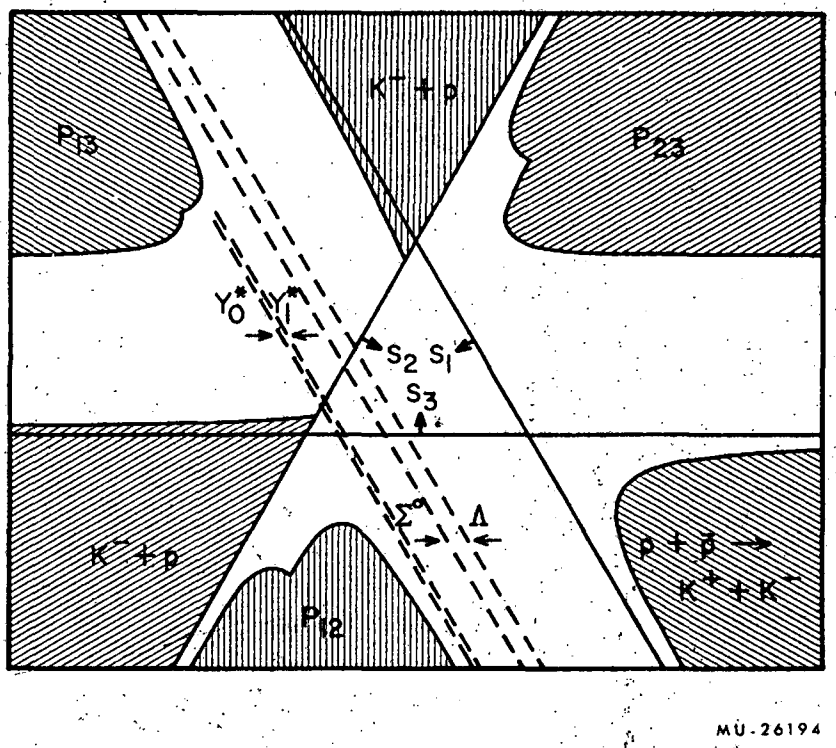

Fig. B2. Mandelstam diagram for the three channels: I, $K^- + p \rightarrow K^- + p$; II, $p + p^- \rightarrow K^+ K^-$; III, $K^+ + p \rightarrow K^+ + p$. Shaded areas define regions where spectral functions are nonvanishing. Dotted lines are poles.

Channel	Particle
I	$\Lambda, \Sigma^0, Y_1^*, Y_0^*$
II	ρ, ω
III	none.

3. Forward dispersion relations. The one-dimensional dispersion relations are derived from the expression (B-2) as follows. First, consider s_1 fixed in its physical energy range. Then we see from Fig. B2 that the other two s variables are "nonphysical". Thus the only denominators which can vanish are those containing $s_1'-s_1$. Using the relation

$$\frac{1}{s_1'-s_1} = P\,\frac{1}{s_1'-s_1} + i\pi\,\delta(s_1'-s_1)\,, \tag{B-3}$$

where P indicates principal value integral, one finds

$$\text{Im } A(s_1, s_2, s_3) = \rho(s_1) + \frac{1}{\pi}\int \frac{\rho_{12}(s_1, s_2')ds_2'}{(s_2'-s_2)} + \frac{1}{\pi}\int \frac{\rho_{13}(s_1, s_3')ds_3'}{(s_3'-s_3)}$$
$$\equiv A_1(s_1, s_2, s_3)\,. \tag{B-4}$$

Similar expressions can be found for A_2 and A_3 where s_2 and s_3, respectively, are confined to physical values. The amplitudes outside the physical regions are now defined by the expressions given for A_1, A_2, and A_3. With this definition the invariant amplitude can be written in three forms in terms of A_1, A_2, and A_3.

We are interested in the form that requires the momentum-transfer variable for K^+-p scattering (s_2) to be fixed, namely

$$A(s_1, s_2, s_3) = \frac{1}{\pi}\int \frac{ds_2'\,\rho_2(s_2')}{(s_2'-s_2)} + \frac{1}{\pi}\int \frac{ds_1'\,A_1(s_1', s_2, s_3')}{(s_1'-s_1)}$$
$$+ \frac{1}{\pi}\int \frac{ds_3'\,A_3(s_1', s_2, s_3')}{(s_3'-s_3)}\,. \tag{B-5}$$

In particular we want dispersion relations for forward scattering where $s_2 = 0$.

Then

$$A(s_1, 0, s_3) = C + \frac{1}{\pi}\int \frac{A_1(s_1', 0, s_3')ds_1'}{(s_1'-s_1)} + \frac{1}{\pi}\int \frac{A_3(s_1', 0, s_3')ds_3'}{(s_3'-s_3)} , \tag{B-6}$$

where

$$C = \frac{1}{\pi}\int \frac{ds_2'\ \rho_2(s_2')}{s_2'-s_2} = \text{constant} .$$

The region of integration below the physical threshold $(M+1)^2$ in the s_1 integral contributes poles at the position indicated previously. Each of the pole terms is of the form $\frac{\Gamma_i}{M_i^2-s_i}$, where Γ_i is the residue of the pole and M_i is the mass of the intermediate state particle associated with the pole. The unphysical region is further complicated by the existence of two-particle intermediate states, which lead to branch points at $s_1 = (M_\Delta + M_\pi)^2$ and $s_1 = (M_\Sigma + M_\pi)^2$. If we remove the pole terms from the s_1 integral the lower limit becomes $(M_\Delta+M_\pi)^2 \equiv s_{\Delta\pi}$. There are no unphysical contributions to the integral over s_3. Thus the lower limit for this integral is $(M_K+M_N)^2 \equiv s_0$.

It is convenient to write the dispersion relations for forward scattering in the lab. system where the proton is at rest and the K has energy

$$\omega = \sqrt{k^2} + 1 \quad (M_K = \hbar = c = 1) .$$

Then

$$s_3 = (p_1+p_2)^2 = M^2 + 1 + 2\omega M,$$

where M = nucleon mass. For K^+-p scattering we have

$$\omega = \frac{s_3-m^2-1}{2M} \equiv \omega^+ \quad \text{for channel III,}$$

and a similar expression for K^--p scattering,

$$\omega = \frac{s_1 - m^2 - 1}{2M} \equiv \omega^- \quad \text{for channel I.}$$

The s_1 and s_3 variables are related by $s_1^2 + s_3^2 = 2(M^2 + 1)$, for $s_2 = 0$. Then

$$\omega^+ = \frac{2(1+M^2)-s_1-M^2-1}{2M} = \frac{1 + M^2 - s_1}{2M} = -\omega^- . \tag{B-7}$$

Define $\omega^+ \equiv \omega$. Then (B-6) is the amplitude for channel III and we can write

$$A_{III}(\omega) = C + \sum_i \frac{\Gamma_i}{M_i^2 - (M^2+1-2M\omega)} + \frac{1}{\pi}\int_{\omega_{\Delta\pi}}^{\infty} \frac{A_1(\omega')d\omega' \; 2M}{(2M\omega' + M^2+1) - (M^2+1-2M\omega)}$$

$$+ \frac{1}{\pi}\int_1^{\infty} \frac{A_3(\omega')d\omega'}{(2M\omega'+M^2+1)-(2M\omega+M^2+1)}$$

$$= \sum_i \frac{\Gamma_i}{2M(\omega_i+\omega)} + \frac{1}{\pi}\int_{\omega_{\Delta\pi}}^{\infty} \frac{A_1(\omega')d\omega'}{\omega'+\omega} + \frac{1}{\pi}\int_1^{\infty} \frac{A_3(\omega')d\omega'}{\omega'-\omega} ,$$

where

$$\omega_i = \frac{M_i^2 - M^2 - 1}{2M} . \tag{B-8}$$

The only term that can have an imaginary part is the integral over A_3, where the denominator vanishes at $\omega_3' = \omega_3$. Using (B-3) we can write the real part of the amplitude for channel III

$$\text{Re } A_{III}(\omega) = C + \sum_i \frac{\Gamma_i}{2M(\omega_i+\omega)} + \frac{1}{\pi}\int_{\omega_{\Delta\pi}}^{\infty} \frac{A_1(\omega')d\omega'}{\omega'+\omega} + \frac{P}{\pi}\int_1^{\infty} \frac{A_3(\omega')d\omega'}{\omega'-\omega} . \tag{B-9}$$

The physical scattering amplitudes are related to the invariant amplitudes by $A(\omega) = \frac{W}{2} f^{c.m.}$, W = total energy in c.m. The physical forward scattering amplitudes for the c.m. and lab systems are related by

$$f_0^L = \frac{k_L}{k_{c.m.}} f_0^{c.m.} = \frac{W}{M} f_0^{c.m.} .$$

Then

$$f_0^L(\omega) = \frac{2}{M} A(\omega) .$$

Defining

$$f_0^L(\pm\omega) \equiv D_\pm(\omega) + i A_\pm(\omega) ,$$

we can write

$$D_\pm(\omega) = C + \sum_i \frac{\Gamma_i}{M^2(\omega_i \pm \omega)} + \frac{1}{\pi}\int_{\omega_{\Lambda\pi}}^{\infty} \frac{A_-(\omega')d\omega'}{\omega' \pm \omega} + \frac{1}{\pi}\int_1^{\infty} \frac{A_+(\omega')d\omega'}{\omega' \mp \omega} . \tag{B-10}$$

4. Pole Terms. It can be shown that the residues at the poles are given by

$$\frac{\Gamma_i}{M^2} = + \frac{g_i^2}{4\pi} \frac{(M_i+M)^2-1}{M M_i} \quad \text{for even (K, i) parity}$$

$$= - \frac{g_i^2}{4\pi} \frac{[1-(M_i-M)^2]}{M M_i} \quad \text{for odd (K, i) parity.}$$

The sum over the pole terms for K-p dispersion relation is

$$\sum \frac{\Gamma_i}{M^2(\omega_i-\omega)} = \frac{1}{M^2}\left[\frac{\Gamma_\Lambda}{(\omega_\Lambda-\omega)} + \frac{\Gamma_\Sigma}{(\omega_\Sigma-\omega)} + \frac{\Gamma_{Y_1^*}}{(\omega_{Y_1^*}-\omega)} + \frac{\Gamma_{Y_0^*}}{(\omega_{Y_0^*}-\omega)}\right],$$

where

$$\omega_\Lambda = 0.125,$$

$$\omega_\Sigma = 0.320,$$

$$\omega_{Y_1^*} = 0.403,$$

$$\omega_{Y_0^*} = 0.429 .$$

For ω sufficiently large we can consider a composite pole having residue $\tilde{\Gamma}$ at $\tilde{\omega} = 0.32$.

5. The unphysical continuum. The branch cuts beginning at $\omega = \omega_{\Delta\pi}$ and $\omega_{\Sigma\pi}$ in the unphysical region introduce a complication into the calculation since the imaginary part of the scattering amplitude cannot be evaluated in a direct way in this region. One can only proceed by extrapolating from the physical region according to some theoretical scheme. One such approach is to use the S-wave zero effective range scattering lengths determined by Dalitz and Tuan[29] to calculate the scattering amplitude in the unphysical region. The S-wave forward scattering amplitude can be written

$$f(0) = \frac{1}{2k}\left[\sin\delta_0 \exp(i\delta_0) + \sin\delta_1 \exp(i\delta_1)\right], \qquad \text{(B-11)}$$

where

δ_0 = S-wave phase shift for T = 0

δ_1 = S-wave phase shift for T = 1.

In terms of the complex scattering lengths given by

$$A = a + i\,b = \frac{1}{k \cot\delta},$$

(B-12) can be written

$$f(0) = \frac{1}{2}\,\frac{A_0 + A_1 - 2\,i\,k\,A_0A_1}{(1 - i\,k\,A_0)(1 - i\,k\,A_1)}. \qquad \text{(B-12)}$$

For ω less than 1, $k = i\,|k|$. We find for the imaginary part of the scattering amplitude

$$\text{Im } f(0) = \frac{1}{2}\left[\frac{b_0}{(1+a_0|k|)^2 + b_0^2|k|^2} + \frac{b_1}{(1+a_1|k|)^2 + b_1^2|k|^2}\right]. \qquad \text{(B-13)}$$

We have used the two sets of scattering lengths found by Humphrey and Ross[30] to calculate (B-13).

6. The high-energy region. The total cross sections for K^--p (σ_-) and K^+-p (σ_+) have been measured up to about $\omega = 40$. The integrals in (B-10) were evaluated by drawing a smooth curve through the experimental values for $A_\pm$, which were calculated by using the optical theorem

$$A_\pm = \frac{\sqrt{\omega^2 - 1}\,\sigma_\pm}{4\pi}$$

and numerically integrating under this curve up to $\omega = 40$. The energy region above $\omega = 40$ can be evaluated by using the expressions given by Udgaonkar,[25]

$$4\pi (A_- - A_+) \approx c\,\omega^{a_1}$$

$$4\pi (A_- + A_+) \approx \omega f + h\,\omega^{a_2}, \text{ for } \omega >> 1 , \qquad \text{(B-14)}$$

where we have set

$$k = \sqrt{\omega^2 - 1} \approx \omega .$$

The integrals in (B-10) can be written

$$I_\pm = \frac{1}{\pi} \int_{\omega_0}^{\infty} \frac{\omega' (A_+ + A_-) \mp \omega (A_- - A_+)\, d\omega'}{(\omega')^2 - \omega^2}$$

These integrals do not converge. Convergent forms can be found by forming subtracted relations. Consider, for example, the single subtraction

$$I_+(\omega_1) - I_+(\omega_2) \approx \frac{1}{4\pi^2} \int_{\omega_0}^{\infty} \left\{ \frac{(\omega_1^2 - \omega_2^2)[\omega' f + (\omega')^{a_2} h] \omega' + (\omega_1 - \omega_2)[(\omega')^2 + \omega_1 \omega_2]}{[(\omega')^2 - \omega_1^2][(\omega')^2 - \omega_1^2]} c(\omega')^{a_1} \right\} d\omega'$$

For $\omega_0 >> \omega_1, \omega_2$ we can write

$$I_+(\omega_1) - I_+(\omega_2) \approx \frac{1}{4\pi^2} \int_{\omega_0}^{\infty} \left\{ \frac{(\omega_1^2 - \omega_2^2)\left[\omega' f + (\omega')^{a_2} h\right] + (\omega_1 - \omega_2)(\omega')^{(2+a_1)}}{\omega'^4} \right\} d\omega'$$

$$= \frac{(\omega_1^2 - \omega_2^2)}{4\pi^2} \left[\frac{f}{\omega_0} + \frac{h}{(2-a_2)(\omega_0)^{(2-a_2)}} \right] - \frac{(\omega_1 - \omega_2)}{4\pi^2} \left[\frac{1}{(1-a_1)(\omega_0)^{(1-a_1)}} \right]$$

REFERENCES

1. C. Franzinetti and G. Morpurgo, Nuovo cimento 6, 469 (1957); R. H. Dalitz, Repts. Progr. in Phys. 20, 163 (1957). Both of these articles describe the early nuclear-emulsion and cloud chamber work.
2. See for example, C. Ceolin and L. Taffara, Nuovo cimento 5, 435 (1957); D. Amati and B. Vitale, Nuovo cimento 5, 1533 (1957); P. T. Matthews and A. Salam, Phys. Rev. 110, 569 (1953); C. Ceolin, V. De Santis and L. Taffara, Nuovo cimento 12, 502 (1959); and G. Bialkowski and A. Jurewicz, Nuclear Phys. 17, 359 (1960).
3. For a recent exposition of the theory, and a collection of reprints of some of the important published work, see G. F. Chew S-Matrix Theory of Strong Interactions (W. A. Benjamin, Inc., New York, 1961).
4. "Proofs" of dispersion relations which have been given in the past have relied on field theoretic methods. See, e. g., R. J. Eden, in Proceedings of the 1960 Annual International Conference on High-Energy Physics at Rochester (Interscience Publishers, Inc., New York, 1960), p. 219.
5. K. Igi, Progr. Theoret. Phys. (Kyoto) 19, 238 (1958).
6. P. T. Matthews and A. Salam Phys. Rev. 110, 569 (1958); C. Goebel, Phys. Rev. 110, 572 (1958); for a summary of the results of these investigations see R. H. Dalitz, in Proceedings of 1958 Annual International Conference on High-Energy Physics, Geneva (CERN, Geneva, 1958).
7. R. Karplus, L. T. Kerth, and T. Kycia, Phys. Rev. Letters 2, 510 (1959).
8. V. Cook, B. Cork, T. F. Hoang, D. Keefe, L. T. Kerth, W. A. Wenzel, and T. F. Zipf, Phys. Rev. 123, 320 (1961).

9. For summary of emulsion data see D. Keefe, A. Kernan, A. Montwill, M. Grilli, L. Guerriero, and G. A. Salandin, Nuovo cimento 12, 241 (1959).
10. T. F. Kycia, L. T. Kerth, and R. G. Baender, Phys. Rev. 118, 553 (1960).
11. G. von Dardel, D. H. Frisch, D. Mermod; R. H. Milburn; P. A. Pirone, M. Vivargent, G. Weber, and K. Winter, Phys. Rev. Letters 5, 333 (1960); H. C. Burrowes, D. O. Caldwell, D. H. Frisch, D. A. Hill, D. M. Ritson, and R. A. Schluter, Phys. Rev. Letters 2, 117 (1959); A. S. Vovenko, B. A. Kulakov, M. F. Lykhachev, A. L. Ljubimimov, J. u. A. Matulenko, I. A. Savin, Y. e. V. Smirnoff, V. S. Stavinsky, Sui Yuin-Chan, and Shzan Nai-Sen, Joint Institute for Nuclear Research, Dubna Report D 721, May 1961 (unpublished).
12. B. Cork, D. Keefe and W. A. Wenzel, Proceedings of International Conference on Instrumentation for High-Energy Physics, Berkeley, 1960 (Interscience Publishers, Inc., New York, 1961), p. 84.
13. V. Cook, D. Keefe, L. T. Kerth, P. G. Murphy, W. A. Wenzel, and T. Zipf, Phys. Rev. Letters 7, 182 (1961).
14. We are grateful to Mr. Carl Noble for carrying out these calculations.
15. R. J. Glauber, Phys. Rev. 100, 242 (1955).
16. For a more complete description of this counter see reference 8.
17. N. F. Mott and H. S. W. Massey, The Theory of Atomic Collisions, 2nd ed. (Oxford University Press, London, 1949), p. 78.
18. J. H. Foote (Ph. D. Thesis), Scattering of Positive Pions on Protons at 310 Mev: Recoil-Nucleon Polarization and Phase-Shift Analysis, Lawrence Radiation Laboratory Report UCRL-9191, Sept. 1960 (unpublished).
19. L. I. Schiff, Quantum Mechanics, 2nd ed. (McGraw-Hill Book Company, New York Inc., 1955), p. 116.
20. F. T. Solmitz, Phys. Rev. 94, 1799 (1954).

21. The program, described by Foote (reference 18), was originally written for π^+-p scattering. Modifications were made for K^+-p scattering and for allowing variation of the absorption parameters.

22. T. F. Stubbs, H. Bradner, W. Chinowsky, G. Goldhaber, S. Goldhaber, W. Slater, D. M. Stork, and H. K. Ticho, Phys. Rev. Letters 7, 188 (1961).

23. D. Amati, M. Fierz, and V. Glaser, Phys. Rev. Letters 4, 89 (1960).

24. This condition was first postulated by I. Ia. Pomeranchuk, J. Exptl. Theoret. Phys. (USSR) 34, 725 (1958) [Soviet Phys. JETP 34(7), 499 (1958)]. It is pointed out in reference 23 that although the rather plausible general arguments employed by Pomeranchuk lead to the conclusion that $\frac{A_{\pm}(\omega)}{\omega}$ is bounded, it is not clear that, if it does not tend to zero, it tends to a limit.

25. B. M. Udgaonkar, Phys. Rev. Letters 8, 142 (1962).

26. G. Goldhaber, S. Goldhaber, and W. Lee (Lawrence Radiation Laboratory, Berkeley), private communication.

27. R. H. Dalitz, in Proceedings of the International Conference on Elementary Particles, Aix-en-Provence, 1961 (Centre d'Etudes Nucleaires, Saclay, France, 1961).

28. R. D. Tripp, M. B. Watson, and M. Ferro-Luzzi, Phys. Rev. Letters 8, 175 (1962).

29. R. H. Dalitz and S. F. Tuan, Ann. Phys. 10, 307 (1960).

30. W. E. Humphrey and R. R. Ross, Low-Energy Interaction of K^- Mesons in Hydrogen Lawrence Radiation Laboratory Report UCRL-10018, Jan. 1962; Phys. Rev. (in press).